IPEM Institute of Physics and Engineering in Medicine

PAPER • OPEN ACCESS

A comprehensive model for x-ray projection imaging system efficiency and image quality characterization in the presence of scattered radiation

To cite this article: P Monnin *et al* 2017 *Phys. Med. Biol.* **62** 5691

View the article online for updates and enhancements.

A comprehensive model for x-ray projection imaging system efficiency and image quality characterization in the presence of scattered radiation

P Monnin[1,5], F R Verdun[1], H Bosmans[2,3], S Rodríguez Pérez[3,4] and N W Marshall[2,3]

[1] Institute of Radiation Physics (IRA), Lausanne University Hospital (CHUV), Rue du Grand-Pré 1, 1007 Lausanne, Switzerland
[2] Department of Radiology, UZ Gasthuisberg, Herestraat 49, 3000 Leuven, Belgium
[3] Medical Imaging Research Center, Medical Physics and Quality Assessment, Katholieke Universiteit Leuven, 3000 Leuven, Belgium
[4] SCK·CEN, Boeretang 200, Mol 2400, Belgium

E-mail: pascal.monnin@chuv.ch

Abstract

This work proposes a method for assessing the detective quantum efficiency (DQE) of radiographic imaging systems that include both the x-ray detector and the antiscatter device. Cascaded linear analysis of the antiscatter device efficiency (DQE_{ASD}) with the x-ray detector DQE is used to develop a metric of system efficiency (DQE_{sys}); the new metric is then related to the existing system efficiency parameters of effective DQE (eDQE) and generalized DQE (gDQE). The effect of scatter on signal transfer was modelled through its point spread function (PSF), leading to an x-ray beam transfer function (BTF) that multiplies with the classical presampling modulation transfer function (MTF) to give the system MTF. Expressions are then derived for the influence of scattered radiation on signal-difference to noise ratio (SDNR) and contrast-detail (c-d) detectability.

The DQE_{sys} metric was tested using two digital mammography systems, for eight x-ray beams (four with and four without scatter), matched in terms of effective energy. The model was validated through measurements of contrast, SDNR and MTF for poly(methyl)methacrylate thicknesses covering the range of scatter fractions expected in mammography. The metric also successfully predicted changes in c-d detectability for different scatter conditions. Scatter

[5] Author to whom any correspondence should be addressed.

fractions for the four beams with scatter were established with the beam stop method using an extrapolation function derived from the scatter PSF, and validated through Monte Carlo (MC) simulations. Low-frequency drop of the MTF from scatter was compared to both theory and MC calculations. DQE_{sys} successfully quantified the influence of the grid on SDNR and accurately gave the break-even object thickness at which system efficiency was improved by the grid. The DQE_{sys} metric is proposed as an extension of current detector characterization methods to include a performance evaluation in the presence of scattered radiation, with an antiscatter device in place.

Keywords: mammography, image quality, scatter fraction, MTF, detective quantum efficiency (DQE), cascaded system analysis, system DQE

(Some figures may appear in colour only in the online journal)

Nomenclature

Symbol	Meaning
AEC	Automatic exposure control
ASD	Anti-scatter device
BTF	Beam transfer function
BTF_{in}	BTF at the ASD input
BTF_{out}	BTF at the ASD output or detector entrance
d'	Detectability index
D	Diameter of a disc (cm)
DAK	Detector air kerma (μGy)
DQE	Detective quantum efficiency
DQE_d	Detector DQE
DQE_{ASD}	DQE of the anti-scatter device (ASD)
DQE_{sys}	System DQE
ΔP_{out}	Object contrast in the image
eDQE	Effective DQE
FWHM	Full width at half maximum
gDQE	Generalized DQE
gMTF	Generalized modulation transfer function
HVL	Half value layer (mm)
MTF	Presampling modulaton transfer function in the image measured without scatter
MTF_{sys}	Presampling modulaton transfer function in the image measured with scatter
f	Spatial frequency (mm^{-1})
G_P	Detector glare due to primary photons
G_S	Detector glare due to scattered photons
G_{P+S}	Detector glare due to primary and scattered photons
K_{in}^P	Air kerma at the ASD input for a beam composed of primary photons only (μGy)
K_{in}^{PS}	Air kerma at the ASD input for a beam composed of primary and scattered photons (μGy)

k_q	Gain factor for quantum noise
μ	Linear attenuation coefficient (cm^{-1})
μ_{Al}	Linear attenuation coefficient of aluminum (cm^{-1})
μ_{Au}	Linear attenuation coefficient of gold (cm^{-1})
NEQ	Noise equivalent quanta (mm^{-2})
NPS	Noise power spectrum measured in the image (μGy^2 mm^2)
NPS$_{in}$	Quantum NPS in the beam at the ASD input (μGy^2 mm^2)
NNPS	Normalized noise power spectrum measured in the image (mm^2)
NNPS$_{in}$	Quantum NNPS in the beam at the ASD input (mm^2)
OTF$_b$	Optical transfer function of the x-ray beam
P_{in}	Air kerma due to primary photons at the ASD input (μGy)
$\tilde{P}_{in}$	Primary photon fluence at the ASD input (mm^{-2})
P_{out}	Air kerma due to primary photons at the ASD output or detector entrance (μGy)
$\tilde{P}_{out}$	Primary photon fluence at the ASD output (mm^{-2})
PMMA	Polymethylmethacrylate
PSF	Point spread function
PSF$_b$	Beam PSF
PV$_Q$	Mean pixel value measured on the linearized image, expressed in DAK values (μGy)
$^+$PV$_Q$	PV$_Q$ obtained with grid in (μGy)
$^-$PV$_Q$	PV$_Q$ obtained with grid out (μGy)
PV$_Q^{ph}$	PV$_Q$ at the centre of a narrow beam collimated by a circular pinhole (μGy)
PV$_Q^{disc}$	PV$_Q$ at the centre of the image of a circular lead disc (μGy)
r	Radius in polar coordinates (cm)
R	Radius of the lead disc (cm)
ROI	Region of interest
σ	Standard deviation of pixel values (μGy)
σ_T	Target standard deviation of pixel values (μGy)
S_{in}	Air kerma due to scattered photons at the ASD input (μGy)
$\tilde{S}_{in}$	Scattered photon fluence at the ASD input (mm^{-2})
S_{obj}	Transfer function of the object
S_{out}	Air kerma due to scattered photons at the ASD output or detector entrance (μGy)
$\tilde{S}_{out}$	Scattered photon fluence at the ASD output or detector entrance (mm^{-2})
SF	Scatter fraction in the x-ray beam
SF$_{in}$	Scatter fraction in the x-ray beam at the ASD input
SF$_{out}$	Scatter fraction in the x-ray beam at the ASD output or detector entrance
SDNR	Signal difference-to-noise ratio
SNR	Signal-to-noise ratio
SNR$_{in}$	Quantum SNR in the beam at the ASD input
SNR$_{out}$	SNR in the image
Σ	ASD selectivity
T	Object thickness (cm)

T_p	Primary transmission of the ASD
T_s	Scatter transmission of the ASD
T_t	Total transmission of the ASD
VTF	Visual transfer function

1. Introduction

Metrics such as presampling modulation transfer function (MTF), noise power spectrum (NPS), noise equivalent quanta (NEQ) and detective quantum efficiency (DQE) describe detector imaging performance (Metz *et al* 1995, Cunningham 2000). Their measurement specifies primary x-ray beams, consistent with the low amounts of scatter present behind antiscatter devices (ASDs) (IEC 2015). Performance evaluation of the ASD is dealt with in separate guidance (IEC 2013). Scattered radiation that reaches the detector decreases contrast and contributes to image noise, and thereby degrades the signal difference-to-noise ratio (SDNR). The recent development of digital breast tomosynthesis (DBT) has opened the way to grid-less imaging in mammography and the need for an extension to image quality metrics that include scatter, or to characterize system performance including the ASD.

Generalized image quality metrics have been developed that include the influence of scattered radiation, magnification and other sources of geometric unsharpness, namely effective DQE (eDQE) (Samei *et al* 2004, 2009) and generalized DQE (gDQE) (Kyprianou *et al* 2004, 2005a) Intended as an extension of the DQE concept to the whole imaging chain, eDQE is evaluated in the presence of typical scattering phantoms and the system antiscatter device (ASD). This is consistent with an earlier extension of DQE by Wagner *et al* (1980) that characterized antiscatter grid performance by defining grid DQE (DQE_a) as the actual SNR^2 at the grid output compared to SNR^2 for a perfect grid that stops all scatter and selects all primary photons. Ideal scatter rejection therefore corresponds to a grid DQE equal to 1.0. Neitzel (1992) used the same approach to define a signal-to-noise ratio improvement factor. Siewerdsen and Jaffray (2000) showed that scatter degrades DQE as an additive noise source and introduced a scatter compensation factor by which the exposure must be increased to compensate for loss in NEQ(0), i.e. SNR^2. The eDQE is based on generalized MTF and NPS parameters measured directly in images acquired with primary and scattered radiation. A broad range of digital radiography systems (Samei *et al* 2005, 2009, Bertolini *et al* 2012) and mammography systems (Salvagnini *et al* 2013) have been characterized with this metric.

Generalized metrics such as gDQE proposed by Kyprianou *et al* (2004, 2005a, 2005b) include scattered radiation and focal spot unsharpness in order to characterize complete imaging system performance. A homogeneous phantom is used as a scatter source and the influence of focal spot, scatter and detector on contrast transfer is characterized using a generalized MTF (gMTF), measured with scatter. The gMTF and generalized NPS (gNPS) were later introduced in an ideal observer model (Kyprianou *et al* 2005b). More recently, Liu *et al* (2014) implemented a Hotelling observer model to calculate c-d curves and evaluate the influence of scatter on detection task.

In this work, we present a novel approach with a linear cascaded system model that describes signal-to-noise ratio (SNR) transfer through the ASD and detector as a rigorous means of extending the standard DQE concept to the full imaging system, including scatter rejection technique. The deleterious effect of scattered radiation on the signal (MTF) is introduced through the beam transfer function (BTF) built up from the scatter PSF. The detective quantum efficiency of the ASD is defined and combined with the standard detector DQE to give the system DQE (DQE_{sys}). The validity of the model is tested through measurements of contrast, SDNR and MTF for poly(methyl)methacrylate (PMMA) thicknesses covering the
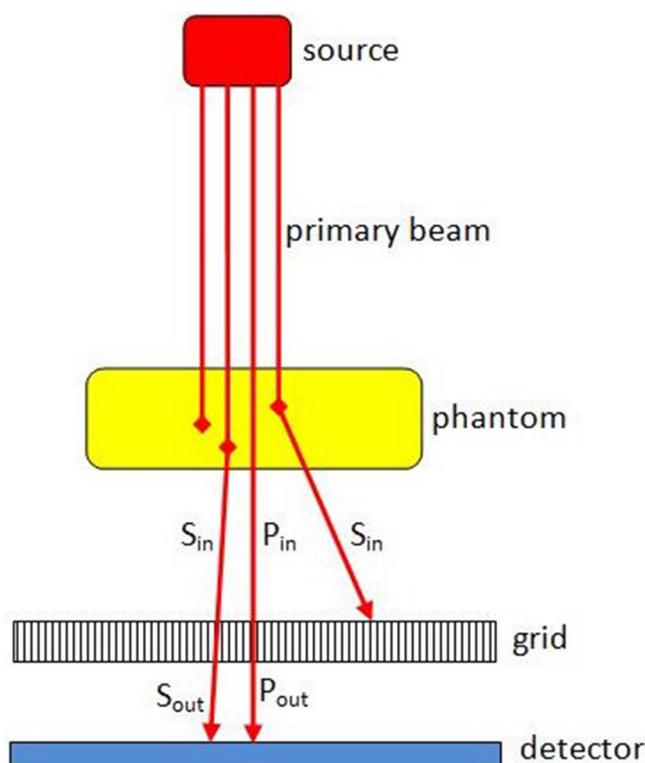
Figure 1. Geometry of irradiation and beam parameters.

range of scatter conditions expected in mammography. In addition, a contrast-detail (c-d) analysis based on the non-prewhitening model observer with eye response (NPWE) was used to predict changes in object detectability for different scatter conditions.

2. Theory

We consider a system composed of detector and ASD (grid, slit or air gap), where P_{in} and S_{in} are the primary and scatter air kerma at the ASD entrance, P_{out} and S_{out} the primary and scatter detector air kerma (DAK), respectively (figure 1). Before the analysis, we note that both eDQE and gDQE have been defined in the object plane, whereas the detector DQE is defined in the detector (or image) plane. The system DQE proposed and developed in this study is calculated in the detector (or image) plane. For purposes of comparison, eDQE and gDQE in this study are also calculated in the detector plane, but the equations can be transformed to the object plane to include magnification effects by shifting the frequencies by the magnification factor between the two planes.

2.1. Effect of scatter on the MTF

The analytical characterization of the spatial distribution of scatter via different scatter point spread functions (PSFs) for medical x-ray imaging systems was initiated by Seibert *et al* (1984) and Boone *et al* (1986). The spatial distribution of x-ray radiation for a (primary) point x-ray source incident on the object can be modelled in the image plane as a beam point spread
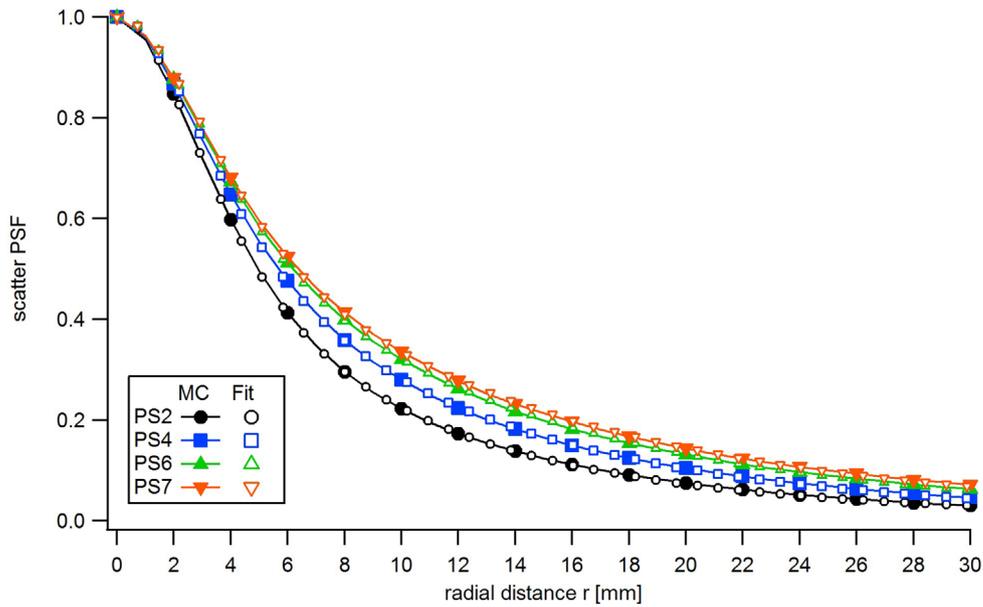
Figure 2. Scatter PSFs obtained by Monte Carlo simulations (MC) for the PS beams with grid out, and fitted curves.

function (PSF_b). Considering a homogeneous (shift invariant) x-ray beam, the beam PSF is independent of the position in the image plane, and the x-ray beam can be computed as the sum of the beam PSF of each point. Functions fitted to scatter PSFs obtained by Monte Carlo simulations were used to assess the PSF of beams with scatter and grid out (equation (1) and figure 2). Due to radial symmetry, the 2D PSF_b were considered in polar coordinates

$$\mathrm{PSF_b}(r) = K_1 \cdot (1 - \mathrm{SF}) \cdot \frac{\delta(r)}{r} + K_2 \cdot \mathrm{SF} \cdot \left(\frac{a}{\left(1 + (r/k_1)^2\right)^{3/2}} + \frac{1-a}{\left(1 + (r/k_2)^2\right)^{3/2}} \right) \cdot$$

$$\tag{1}$$

Where r is the radial distance from the origin, K_1 and K_2 are normalization constants, the Dirac function $\delta(r)/r$ represents the primary beam while the second term is the scatter PSF, SF is the scatter fraction in the beam, and the coefficients a, k_1 and k_2 determine the shape of the scatter distribution. The optical transfer function of the x-ray beam (OTF_b) is the Fourier transform of PSF_b. We define the x-ray beam transfer function (BTF) as the modulus of OTF_b normalized to 1.0 at the zero frequency. The derivation of OTF_b and BTF is given in appendix A.

$$\mathrm{BTF}(f) = (1 - \mathrm{SF}) + \mathrm{SF} \cdot \frac{ak_1^2 \exp(-2\pi k_1 f) + (1-a)\, k_2^2 \exp(-2\pi k_2 f)}{ak_1^2 + (1-a)\, k_2^2}$$

$$\tag{2}$$

The system MTF (MTF_{sys}) measured with scatter in the image plane is the product of the presampling MTF (MTF), i.e. the detector and focal spot blurs, and the BTF at the ASD output (BTF_{out}).

$$\mathrm{MTF_{sys}}(f) = \mathrm{BTF_{out}}(f) \cdot \mathrm{MTF}(f):$$

$$\mathrm{MTF_{sys}}(f) = \left(1 - \mathrm{SF_{out}} + \mathrm{SF_{out}} \cdot \frac{ak_1^2 \exp(-2\pi k_1 f) + (1-a)k_2^2 \exp(-2\pi k_2 f)}{ak_1^2 + (1-a)k_2^2}\right) \cdot \mathrm{MTF}(f) \tag{3a}$$

$$\text{MTF}_{\text{sys}}(f) \cong (1 - \text{SF}_{\text{out}}) \cdot \text{MTF}(f) \text{ for } f > 1/k = \max(1/k_1; 1/k_2) \quad (3b)$$

where $\text{SF}_{\text{out}} = S_{\text{out}}/(P_{\text{out}} + S_{\text{out}})$ is the scatter fraction in the output image (or at the ASD output). The scatter term of BTF_{out} drops quickly to zero at very low frequency, between 0 and $1/k$. As already shown in previous studies (Salvagnini *et al* 2012, 2013), the multiplication of presampling MTF by $(1 - \text{SF}_{\text{out}})$ gives the system MTF for all frequencies above $1/k$. Scattered radiation therefore decreases the signal by $(1 - \text{SF}_{\text{out}})$ for all spatial frequencies important for object/target detection within an image and acts practically as a factor that reduces contrast without modifying the intrinsic sharpness of the imaging system. For $f > 1/k$, the signal in the output image contains only primary photons:

$$(S_{\text{out}} + P_{\text{out}}) \cdot \text{MTF}_{\text{sys}}(f) \cong (S_{\text{out}} + P_{\text{out}})(1 - \text{SF}_{\text{out}}) \cdot \text{MTF}(f) = P_{\text{out}} \cdot \text{MTF}(f) \quad (4)$$

where the relation $\frac{P_{\text{out}}}{P_{\text{out}} + S_{\text{out}}} = 1 - \text{SF}_{\text{out}}$ has been used. Equation (4) shows that scatter contributes to very low frequency signal only within a narrow frequency bandwidth, decreasingly between 0 and $1/k$.

2.2. Effect of scatter on the NEQ

The input noise equivalent quanta (NEQ_{in}) describes the signal-to-noise ratio squared (image quality) at the ASD entrance.

$$\text{NEQ}_{\text{in}}(f) = \frac{(P_{\text{in}} + S_{\text{in}})^2 \cdot \text{BTF}_{\text{in}}^2(f)}{\text{NPS}_{\text{in}}} = \frac{\text{BTF}_{\text{in}}^2(f)}{\text{NNPS}_{\text{in}}} = (\tilde{P}_{\text{in}} + \tilde{S}_{\text{in}}) \cdot \text{BTF}_{\text{in}}^2(f) \quad (5)$$

$P_{\text{in}} + S_{\text{in}}$ is the input air kerma (in μGy) at the ASD entrance. Quantum noise in the x-ray beam is made of primary and scattered photons. NPS_{in} is the quantum noise power spectrum at the ASD input expressed in $\mu\text{Gy}^2 \cdot \text{mm}^2$ (IEC 2015), and NNPS_{in} is the NPS_{in} normalized by the mean signal squared: $\text{NNPS}_{\text{in}} = \text{NPS}_{\text{in}}/(P_{\text{in}} + S_{\text{in}})^2$. Quantum NNPS_{in} is expressed in mm^2 and follows Poissonian statistics. It is therefore a white noise whose amplitude is directly linked to $\tilde{P}_{\text{in}} + \tilde{S}_{\text{in}}$, the photon fluence (photons mm^{-2}) at the ASD input: $\text{NNPS}_{\text{in}} = 1/(\tilde{P}_{\text{in}} + \tilde{S}_{\text{in}})$.

The model we propose considers the ASD as a photon selector characterized by primary and scatter transmissions, without introducing correlations in noise (Chan *et al* 1990). Hence, the NPS at the ASD output (NPS_{out}) is white and determined by the photon fluence ($\tilde{P}_{\text{out}} + \tilde{S}_{\text{out}}$ photons mm^{-2}) at the ASD output (and in the output image). The NEQ at the ASD output is given by equation (6):

$$\text{NEQ}_{\text{out}}(f) = \frac{(P_{\text{out}} + S_{\text{out}})^2 \cdot \text{BTF}_{\text{out}}^2(f)}{\text{NPS}_{\text{out}}} = \frac{\text{BTF}_{\text{out}}^2(f)}{\text{NNPS}_{\text{out}}} = (\tilde{P}_{\text{out}} + \tilde{S}_{\text{out}}) \cdot \text{BTF}_{\text{out}}^2(f) \quad (6)$$

The MTF and NPS shapes are modified by the detector, and the NEQ in the image is spatial-frequency dependent:

$$\text{NEQ}(f) = \frac{(P_{\text{out}} + S_{\text{out}})^2 \cdot \text{MTF}_{\text{sys}}^2(f)}{\text{NPS}(f)} = \frac{\text{MTF}_{\text{sys}}^2(f)}{\text{NNPS}(f)} \quad (7)$$

These general expressions for NEQs can be simplified for all spatial frequencies important for object/target detection ($f > 1/k$).

Particular case for $f > 1/k$:

Using $\mathrm{BTF} \cong 1 - \mathrm{SF}$ (equation (3*b*)) and $\frac{\tilde{P}}{\tilde{P}+\tilde{S}} = 1 - \mathrm{SF}$, the NEQs can be simplified to:

$$\mathrm{NEQ_{in}} \cong \left(\tilde{P}_{\mathrm{in}} + \tilde{S}_{\mathrm{in}}\right) \left(1 - \mathrm{SF_{in}}\right)^2 = \tilde{P}_{\mathrm{in}} \cdot \left(1 - \mathrm{SF_{in}}\right) \tag{8}$$

$$\mathrm{NEQ_{out}} \cong \left(\tilde{P}_{\mathrm{out}} + \tilde{S}_{\mathrm{out}}\right) \left(1 - \mathrm{SF_{out}}\right)^2 = \tilde{P}_{\mathrm{out}} \cdot \left(1 - \mathrm{SF_{out}}\right) \tag{9}$$

$$\mathrm{NEQ}\left(f\right) \cong \left(1 - \mathrm{SF_{out}}\right)^2 \cdot \frac{\mathrm{MTF}^2\left(f\right)}{\mathrm{NNPS}\left(f\right)} \tag{10}$$

The fraction of scattered radiation in the output image ($\mathrm{SF_{out}}$) reduces the NEQ by $\left(1 - \mathrm{SF_{out}}\right)^2$. This loss in NEQ due to scatter can be offset by an increase in DAK of $\left(1 - \mathrm{SF_{out}}\right)^{-2}$, termed the scatter compensation factor in Siewerdsen and Jaffray (2000). The NEQ in the absence of scatter is a particular case where $\mathrm{SF} = 0$. The notation NEQ in our study is therefore used irrespective of the presence or absence of scatter.

2.3. Metrics of imaging system efficiency with scatter

2.3.1. System DQE (DQE$_{sys}$). Cascaded linear analysis has been successfully used to provide comprehensive descriptions of detector DQE by modelling the signal and noise transfer as successive gain and blurring stages (Rabbani *et al* 1987, Siewerdsen *et al* 1997, Zhao and Rowlands 1997, Cunningham and Shaw 1999, Cunningham *et al* 2004, Kim 2006, Hunt *et al* 2007, Monnin *et al* 2016). In this study, cascaded system analysis is applied to a system composed of detector and ASD (grid, slit or air gap) (figure 1). The DQE describes the ability of the imaging device to preserve the SNR present in the radiation field in the resulting image (Shaw 1978, IEC 2015). We therefore define the DQE for the different elements of the imaging system as the efficiency of SNR^2 (NEQ) transfer through these elements. For the ASD, we define T_{p}, T_{s} and T_{t} as the primary, scatter and total transmissions of the ASD, respectively:

$$T_{\mathrm{p}} = \frac{\tilde{P}_{\mathrm{out}}}{\tilde{P}_{\mathrm{in}}} = \frac{P_{\mathrm{out}}}{P_{\mathrm{in}}} \tag{11a}$$

$$T_{\mathrm{s}} = \frac{\tilde{S}_{\mathrm{out}}}{\tilde{S}_{\mathrm{in}}} = \frac{S_{\mathrm{out}}}{S_{\mathrm{in}}} \tag{11b}$$

$$T_{\mathrm{t}} = \frac{\tilde{P}_{\mathrm{out}} + \tilde{S}_{\mathrm{out}}}{\tilde{P}_{\mathrm{in}} + \tilde{S}_{\mathrm{in}}} = \frac{P_{\mathrm{out}} + S_{\mathrm{out}}}{P_{\mathrm{in}} + S_{\mathrm{in}}} = T_{\mathrm{p}} - \left(T_{\mathrm{p}} - T_{\mathrm{s}}\right) \cdot \mathrm{SF_{in}} \tag{11c}$$

The ASD DQE (DQE$_{\mathrm{ASD}}$) is defined as:

$$\mathrm{DQE_{ASD}}\left(f\right) = \frac{\mathrm{NEQ_{out}}\left(f\right)}{\mathrm{NEQ_{in}}\left(f\right)} = \frac{\tilde{P}_{\mathrm{out}} + \tilde{S}_{\mathrm{out}}}{\tilde{P}_{\mathrm{in}} + \tilde{S}_{\mathrm{in}}} \cdot \frac{\mathrm{BTF}^2_{\mathrm{out}}\left(f\right)}{\mathrm{BTF}^2_{\mathrm{in}}\left(f\right)} = T_{\mathrm{t}} \cdot \frac{\mathrm{BTF}^2_{\mathrm{out}}\left(f\right)}{\mathrm{BTF}^2_{\mathrm{in}}\left(f\right)} \tag{12}$$

DQE$_{\mathrm{ASD}}$ describes the variation in NEQ due to the use of the ASD, without changing patient dose. It depends on the SNR balance between the primary absorption and scatter rejection of the ASD; this is greater than 1.0 if the ASD increases the SNR and lower than 1.0 otherwise. In the absence of an ASD, DQE$_{\mathrm{ASD}}$ is neutral, i.e. DQE$_{\mathrm{ASD}} = 1$.

The detector DQE (DQE$_{\mathrm{d}}$) is defined as the ratio between NEQ(f) in the output image and NEQ$_{\mathrm{out}}$(f) at the detector entrance (equations (6) and (7)):

$$\mathrm{DQE_d}\,(f) = \frac{\mathrm{NEQ}\,(f)}{\mathrm{NEQ_{out}}\,(f)} = \frac{\mathrm{MTF^2_{sys}}\,(f)}{\mathrm{BTF^2_{out}}\,(f) \cdot \mathrm{NNPS}\,(f) \cdot \left(\tilde{P}_{out} + \tilde{S}_{out}\right)} \tag{13}$$

We define system DQE ($\mathrm{DQE_{sys}}$) as the efficiency of $\mathrm{SNR^2}$ (NEQ) transfer through the imaging system, given in the cascaded model by the product of $\mathrm{DQE_{ASD}}$ and $\mathrm{DQE_d}$:

$$\mathrm{DQE_{sys}}\,(f) = \mathrm{DQE_{ASD}}\,(f) \cdot \mathrm{DQE_d}\,(f) = \frac{\mathrm{MTF^2_{sys}}\,(f)}{\mathrm{BTF^2_{in}}\,(f) \cdot \mathrm{NNPS}\,(f) \cdot \left(\tilde{P}_{in} + \tilde{S}_{in}\right)} \tag{14}$$

These general expressions for DQEs can be simplified for all spatial frequencies important for object/target detection ($f > 1/k$).

Particular case for $f > 1/k$:
Using equations (8), (9), (11a) and (11c) and again the relation $\frac{\tilde{P}}{\tilde{P}+\tilde{S}} = 1 - \mathrm{SF}$, $\mathrm{DQE_{ASD}}$ can be expressed as a function of T_{p} and T_{t}:

$$\mathrm{DQE_{ASD}} = \frac{\mathrm{NEQ_{out}}}{\mathrm{NEQ_{in}}} = \frac{\tilde{P}_{out}}{\tilde{P}_{in}} \cdot \frac{1 - \mathrm{SF_{out}}}{1 - \mathrm{SF_{in}}} = \frac{T^2_{\mathrm{p}}}{T_{\mathrm{t}}} \tag{15a}$$

The ASD DQE can also be expressed as a function of the ASD selectivity ($\Sigma = T_{\mathrm{p}}/T_{\mathrm{s}}$):

$$\mathrm{DQE_{ASD}} = \frac{T_p \cdot \Sigma}{\Sigma - (\Sigma - 1) \cdot \mathrm{SF_{in}}} \tag{15b}$$

The primary transmission (numerator) is linked to the change in (primary) signal and the denominator to the noise level. The square root of this factor was introduced by Neitzel (1992) as the ratio of SNR of images acquired with and without grid, named the SNR improvement factor (K_{SNR}). This is equivalent to the factors K_{SDNR} or SIF used in later studies (Shen *et al* 2006, Carton *et al* 2009, Chen *et al* 2015) and used in IEC 60627 (IEC 2013) to characterize the ability of the grid to improve SDNR or SNR. A perfect ASD with $(T_{\mathrm{p}};T_{\mathrm{s}}) = (1;0)$ would lead to the highest $\mathrm{DQE_{ASD}} = (1 - \mathrm{SF_{in}})^{-1}$.

Using equation (3b), the detector DQE and system DQE can be expressed as follows:

$$\mathrm{DQE_d}\,(f) = \frac{\mathrm{MTF^2_{sys}}\,(f)}{\mathrm{NNPS}\,(f) \cdot \tilde{P}_{out} \cdot (1 - \mathrm{SF_{out}})} = \frac{\mathrm{MTF^2}\,(f)}{\mathrm{NNPS}\,(f) \cdot \left(\tilde{P}_{out} + \tilde{S}_{out}\right)} \tag{16}$$

$$\mathrm{DQE_{sys}}\,(f) = \frac{\mathrm{MTF^2_{sys}}\,(f)}{\mathrm{NNPS}\,(f) \cdot \tilde{P}_{in} \cdot (1 - \mathrm{SF_{in}})} = \frac{T^2_{\mathrm{p}}}{T_{\mathrm{t}}} \cdot \frac{\mathrm{MTF^2}\,(f)}{\mathrm{NNPS}\,(f) \cdot \left(\tilde{P}_{out} + \tilde{S}_{out}\right)} \tag{17}$$

In the absence of an ASD, $\mathrm{DQE_{sys}}$ reverts to $\mathrm{DQE_d}$. Therefore, $\mathrm{DQE_{sys}}$ is higher or lower than $\mathrm{DQE_d}$, depending on the ability of the ASD to modify the SNR.

2.3.2. Effective DQE (eDQE). Following from its definition (Samei *et al* 2004, 2009), the eDQE for a frequency *f* at the detector plane is given by:

$$\mathrm{eDQE}\,(f) = \frac{(1 - \mathrm{SF_{out}})^2 \cdot \mathrm{MTF^2}\,(f)}{\mathrm{NNPS}\,(f) \cdot \tilde{P}_{in}} = T_{\mathrm{p}} \cdot (1 - \mathrm{SF_{out}}) \cdot \mathrm{DQE_d}\,(f) \tag{18a}$$

The eDQE is the NEQ normalized by $\tilde{P}_{in}$, the $\mathrm{NEQ_{in}}$ for an ideal beam with only primary photons:

Table 1. Conversion factors between the efficiency metrics.

To convert To From	DQE_d	DQE_{sys}	$eDQE$	$gDQE$
NEQ	$\tilde{P}_{out}^{-1} \cdot (1 - SF_{out})^{-1}$	$\tilde{P}_{in}^{-1} \cdot (1 - SF_{in})^{-1}$	$\tilde{P}_{in}^{-1}$	$\left(\tilde{P}_{out} + \tilde{S}_{out}\right)^{-1}$
DQE_d	1	T_p^2/T_t	$T_p^2 (1 - SF_{in})/T_t$	$T_p^2 (1 - SF_{in})^2/T_t^2$
DQE_{sys}	T_t/T_p^2	1	$(1 - SF_{in})$	$(1 - SF_{in})^2/T_t$
$eDQE$	$T_t/\left(T_p^2 (1 - SF_{in})\right)$	$(1 - SF_{in})^{-1}$	1	$(1 - SF_{in})/T_t$
$gDQE$	$T_t^2/\left(T_p^2 (1 - SF_{in})^2\right)$	$T_t/(1 - SF_{in})^2$	$T_t/(1 - SF_{in})$	1

$$eDQE(f) = \frac{NEQ(f)}{\tilde{P}_{in}} \tag{18b}$$

This gives eDQE equal to 1.0 for a perfect system composed of a perfect detector (that does not add noise) and a perfect ASD defined by $(T_p; T_s) = (1; 0)$. The eDQE can be only lower than DQE_d for a real ASD.

2.3.3. Generalized DQE (gDQE).

Turning to the gDQE proposed by Kyprianou *et al* (2004, 2005a), signal is taken to be the gMTF, a parameter that characterizes blurring from the detector, focal spot and scatter. The gMTF is equivalent to the system MTF (MTF_{sys}), and using equation (3b) gives:

$$gDQE(f) = \frac{gMTF^2(f)}{NNPS(f) \cdot \left(\tilde{P}_{out} + \tilde{S}_{out}\right)} \cong \frac{(1 - SF_{out})^2 \cdot MTF^2(f)}{NNPS(f) \cdot \left(\tilde{P}_{out} + \tilde{S}_{out}\right)} = (1 - SF_{out})^2 \cdot DQE_d(f) \tag{19a}$$

The gDQE is the NEQ normalized by the total photon fluence at the detector, and is therefore different from the eDQE:

$$gDQE(f) \cong \frac{NEQ(f)}{\tilde{P}_{out} + \tilde{S}_{out}} \tag{19b}$$

Like eDQE, gDQE reverts to DQE_d for a perfect ASD and is equal to 1.0 for a perfect system, but scales differently compared to eDQE.

2.3.4. Links between DQE$_{sys}$, eDQE and gDQE (table 1 and figure 3).

Useful links between the different efficiency metrics are given in table 1 for the case where $f > 1/k$ (validity range of equation (3b)). Compared to the ideal input beam without scatter considered in Wagner *et al* (1980) and Samei *et al* (2009) for eDQE, DQE_{sys} uses the real scatter fraction at the ASD entrance (SF_{in}). The eDQE and gDQE are proportional to the detector and ASD DQEs, but decrease with SF_{in}, mixing efficiency (DQE) with image quality (NEQ). The system DQE depends only on the ASD and detector DQEs, and is therefore a pure imaging system efficiency metric. The DQE_{sys} follows the ASD efficiency (DQE_{ASD}) and increases with SF_{in}. The eDQE and gDQE can be only lower than DQE_d, whereas DQE_{sys} can be higher or lower than DQE_d, depending on DQE_{ASD}. This is clearly illustrated when plotting the metrics as a function of SF_{in} for a theoretical ASD with $T_p = 0.7$ and $T_s = 0.2$ (figure 3).
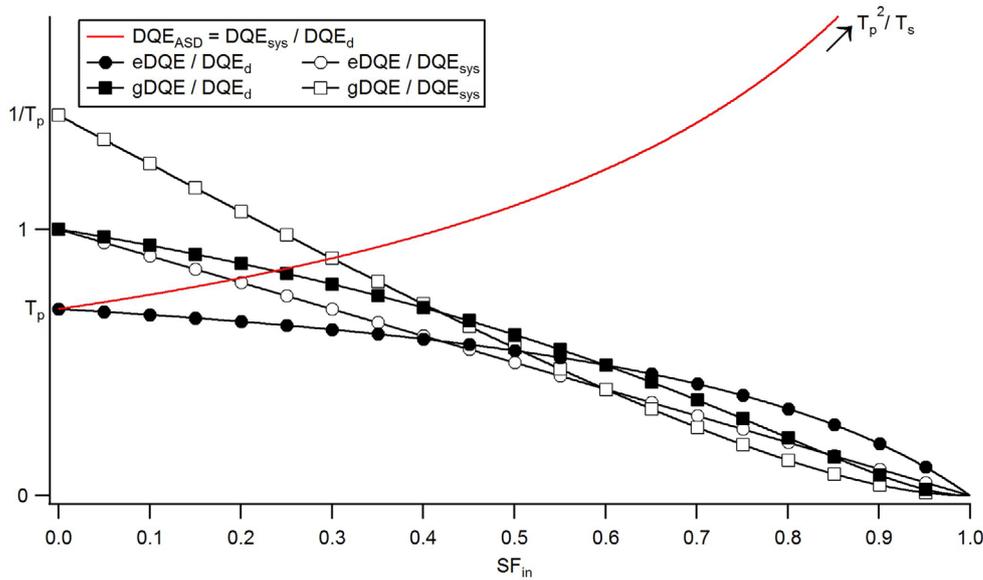
Figure 3. Ratios DQE$_{sys}$/DQE$_d$, e/gDQE/DQE$_d$ and e/gDQE/DQE$_{sys}$ as a function of SF_{in} for a theoretical ASD with $T_p = 0.7$ and $T_s = 0.2$.

2.4. SDNR and contrast-detail analysis with scatter

Considering a thin object of thickness T and linear attenuation coefficient μ in a homogeneous material, the object contrast in the image ΔP_{out}, expressed as a difference in primary signal between the object and the background, will be proportional to the primary DAK in the image background (P_{out}).

$$\Delta P_{out} = P_{out} \left(1 - \exp\left(-\mu T\right)\right) \cong \mu T P_{out} \tag{20}$$

For a quantum noise limited system, the standard deviation of pixel values is proportional to the square root of the DAK, $\sigma = k_q \sqrt{P_{out} + S_{out}}$, where k_q is a gain factor. Under these assumptions, SDNR increases with the square root of the DAK but decreases with the scatter fraction in the image by the factor $(1 - SF_{out})$.

$$\mathrm{SDNR} = \frac{\Delta P_{out}}{\sigma} \cong \frac{\mu T P_{out}}{k_q \sqrt{P_{out} + S_{out}}} = \frac{\mu T}{k_q} \left(1 - SF_{out}\right) \sqrt{P_{out} + S_{out}} \tag{21}$$

The deleterious effect of scatter on the visibility of details such as microcalcifications in mammography can be addressed through the threshold contrast thickness of details. The CDMAM phantom is often used for this purpose. Detectability can be predicted with a good precision with a non-prewhitened model observer with eye filter (NPWE) (Monnin *et al* 2011, Liu *et al* 2014). The detectability index d', known to be a predictive value of object visibility, is calculated from the following parameters: object contrast (signal difference ΔP_{out}) and NPS (both measured with scatter), presampling MTF (measured without scatter), object Fourier signal function (S_{obj}), and the visual transfer function (VTF) (equation (22a)).

$$d' = \frac{\Delta P_{\text{out}}}{\sigma} \underbrace{\frac{\sqrt{2\pi} \int_0^{f_c} S_{\text{obj}}^2 (f) \cdot \text{MTF}^2 (f) \cdot \text{VTF}^2 (f) f \, \mathrm{d}f}{\sqrt{\int_0^{f_c} S_{obj}^2 (f) \cdot \text{MTF}^2 (f) \cdot \text{VTF}^4 (f) \cdot \frac{\text{NPS} (f)}{\sigma^2} f \, \mathrm{d}f}}}_{\cong \kappa D^{\alpha}} \cong \kappa \frac{\Delta P_{\text{out}}}{\sigma} D^{\alpha} \tag{22a}$$

Equation (4) shows that the primary signal difference ΔP_{out} should be used with the presampling MTF in equation (22a). Using MTF_{sys} instead of MTF without modification of equation (22a) would hence underestimate the object detectability. MTF_{sys} can be used along with the normalized object contrast ($\Delta P_{\text{out}}/P_{\text{out}}$) and the NNPS (equation (22b)).

$$d' = \frac{\Delta P_{\text{out}}/P_{\text{out}}}{\sigma} \frac{\sqrt{2\pi} \int_0^{f_c} S_{\text{obj}}^2 (f) \cdot \text{MTF}_{\text{sys}}^2 (f) \cdot \text{VTF}^2 (f) f \, \mathrm{d}f}{\sqrt{\int_0^{f_c} S_{\text{obj}}^2 (f) \cdot \text{MTF}_{\text{sys}}^2 (f) \cdot \text{VTF}^4 (f) \cdot \frac{\text{NNPS} (f)}{\sigma^2} f \, \mathrm{d}f}} \tag{22b}$$

Equation (22a) can be approximated for gold discs of different diameters D as the product between the SDNR ($\Delta P_{\text{out}}/\sigma$) and the factor κD^{α}, where κ depends on the frequency content of signal and NPS, whose shapes are practically independent of detector air kerma in a quantum limited dose range: α is a power parameter depending on the object shape that has to be adjusted to the data.

Using equations (20) and (22a), the c-d curves of a given imaging system for gold discs of diameters D and attenuation coefficient μ_{Au} will satisfy:

$$\mu_{\text{Au}} (1 - \text{SF}_{\text{out}}) \sqrt{P_{\text{out}} + S_{\text{out}}} \cdot D^{\alpha} T = \text{const} \tag{23a}$$

or

$$\log \left(\mu_{\text{Au}} (1 - \text{SF}_{\text{out}}) \sqrt{P_{\text{out}} + S_{\text{out}}} \cdot T \right) = \text{const} - \alpha \log D \tag{23b}$$

The c-d curves given in equations (23a) or (23b) show the threshold gold thickness of CDMAM (T) grows by $(1 - \text{SF}_{\text{out}})^{-1}$ compared to the same DAK without scatter. This loss in detectability due to scatter can be offset by an increase in DAK of $(1 - \text{SF}_{\text{out}})^{-2}$, the scatter compensation factor introduced in Siewerdsen and Jaffray (2000).

3. Material and methods

3.1. Imaging systems

For the practical measurements, two mammography systems were used in this study, a Siemens Inspiration and a Hologic Selenia Dimensions. Both are flat panel (FP) type detectors that employ an amorphous selenium (a-Se) x-ray converter layer coupled to TFT array with a pixel spacing of 70 μm and 85 μm for the Hologic and Siemens units, respectively. The Siemens system has a standard linear grid with a ratio of 5:1 and strip density of 31 lines cm^{-1} while the hologic has a high transmission cellular grid (HTC) with a ratio of 4:1 spaced at 23 lines cm^{-1}. The source-to-image receptor (SID) for the Siemens is 650 mm, while for the Hologic this distance is 700 mm. Source to breast support table distances (STD) are 633 mm and 675 mm for the Siemens and Hologic, respectively. Images used for measurements were DICOM 'For Processing' type.

Table 2. Characteristics of the x-ray beams.

Beam	Filter (mm) PMMA	Al	Effective energy (keV)	HVL (mm Al)	$(\tilde{P}_{out} + \tilde{S}_{out})/DAK$ (mm^{-2} μGy^{-1})	μ of gold (cm^{-1})	μ of aluminium (cm^{-1})
P2	—	1.5	20.75	0.76	6010	0.831	3.138
P4	—	2.5	21.33	0.83	6438	0.766	3.107
P6	—	3.5	21.78	0.90	6763	0.721	3.084
P7	—	4.0	21.98	0.92	6903	0.702	3.073
PS2	20	0.5	20.77	0.75	6031	0.830	3.137
PS4	40	0.5	21.36	0.83	6460	0.765	3.105
PS6	60	0.5	21.81	0.89	6786	0.720	3.082
PS7	70	0.5	22.01	0.92	6926	0.702	3.072

3.2. Beam quality and target standard deviation

First, in comparing these metrics, the x-ray beams were chosen to keep the change in effective energy to a minimum; this holds detector DQE as close to constant as feasible and thus highlights changes in image quality/system efficiency due to changing scatter content or system composition (e.g. adding a component such as a grid). Two types of x-ray beams were used: 'primary' beams (P) with a low scattered x-ray photon content and 'primary + scatter' beams (PS) that reflect the range of SF typically seen in mammography. The experiments using the PS beams were performed for grid-in and grid-out geometries while the P beams used only the grid-in position. The PS beams used the following PMMA thicknesses positioned on the breast support table: 20 mm, 40 mm, 60 mm and 70 mm. These beams are referred to as PS2, PS4, PS6 and PS7—see table 2. The CDMAM phantom was always positioned on top of 20 mm PMMA; any additional PMMA was placed on top of the CDMAM. At typical mammography energies, the CDMAM transmission is equivalent to 10 mm PMMA or 0.5 mm Al (CDMAM manual, Artinis). Hence the CDMAM phantom was replaced in the PMMA stack by a homogeneous (uniform) 0.5 mm Al sheet (>99% purity) of dimension 180 mm × 240 mm for the contrast, MTF and NPS calculations. For P beams, the CDMAM or homogeneous (0.5 mm Al) phantom was supported at a height of 20 mm above the breast support table using small plastic blocks.

Following the method in the IEC standard for DQE measurement, the P beams were generated using Al sheets (>99% purity) positioned at the x-ray tube exit port, with the compression paddle removed, and matched to the PS beams via measured HVLs (table 2). Thicknesses of 20 mm, 40 mm, 60 mm and 70 mm PMMA were simulated with 1 mm, 2 mm, 3 mm and 3.5 mm Al, respectively, referred to as P2, P4, P6 and P7—see table 2.

The W/Rh A/F setting was selected as this is used for a broad range of breast thicknesses on both systems. Tube voltage was set to 29 kV for all acquisitions as this is approximately at the centre of the clinical range (typically 25 kV–32 kV) and enabled selection of tube current-time products (mAs) that gave the chosen target (fixed) standard deviation (σ_T). In this study, standard deviation in the non-linearized images was held constant with changing phantom thickness, as this mimics the behaviour of most AEC devices, where mean pixel value (and standard deviation) is held constant as object thickness is changed (Salvagnini *et al* 2015). The standard deviation obtained for the PS4 beam under automatic exposure control (AEC) was taken as σ_T for the four PS beams with grid out and four P beams for the two mammography systems. For the PS beams with grid in, the mAs settings obtained for the grid out measurements were used. The standard deviation was measured in a 5 mm × 5 mm region of interest (ROI) at the standard position (60 mm from the chest wall edge, centred left-right (EC 2006)).

3.3. Detector response function

Detector response for both systems was measured using a beam quality of 29 kV, W/Rh with grid out. The Al filters were positioned at the tube exit position and a calibrated dosemeter positioned at the standard position (EC 2006) used to estimate detector air kerma (DAK). Four response functions were measured, using filter thicknesses of 1.5 mm, 2.5 mm, 3.5 mm and 4.0 mm Al. Detailed information on the measurements is given in Monnin *et al* (2014). The linearized pixel values expressed in DAK values (DAK $= P_{out} + S_{out}$) were used for contrast, SDNR, MTF and NPS calculations.

3.4. Modulation transfer function (MTF)

A version of the angled edge method was used to measure both the MTF and MTF_{sys} (Samei *et al* 1998). For P beams, the edge was supported at a height of 20 mm above the breast support table using small plastic blocks. Measuring the MTF at 20 mm above the table gave an estimate of sharpness at the position of the CDMAM phantom. A 0.8 mm thick steel edge of dimension 120 mm $\times$ 60 mm was used for the Siemens data while a square tungsten edge of side 50 mm and thickness 0.5 mm was used with the Hologic system. The $MTFs_{sys}$ were measured using the scatter beams (PS2, PS4, PS6 and PS7), with the edge always positioned on 20 mm PMMA + 0.5 mm Al. A 1.0 mm thick copper square of side 200 mm was used for the Siemens data while a 1.0 mm thick copper edge of dimension 120 mm $\times$ 80 mm was used with the Hologic system. For all the P and PS beams, the mAs was adjusted to give a DAK of ~200 μGy. Two images were acquired for each condition studied, and hence the final MTF or MTF_{sys} curves were averaged from two measurements. An ROI side of 40 mm was used to generate the ESF for the P beams, while an ROI of side 100 mm was used for the ESF for the PS beams. Calculation steps for the MTF are described in Monnin *et al* (2016).

3.5. Noise power spectrum (NPS)

Three images of the homogenous phantom were acquired with the mAs values established to give σ_T for the P beams (P2, P4, P6 and P7) with grid in and for the PS beams (PS2, PS4, PS6 and PS7) with grid out. For the PS beams with grid in, the mAs settings derived for the grid out measurements were used. From these homogeneous images, the NPS was calculated using half-overlapping 256 $\times$ 256 pixel ROIs. Details of the NPS implementation are given in Monnin *et al* (2014). The final NPS curves were a radial average of the NPS, excluding the 0° and 90° axial values.

3.6. Contrast and SDNR measurements

The contrast was assessed with a 5 $\times$ 5 $\times$ 0.2 mm Al plate (purity of 99.5%) positioned at the reference point at a height of 20 mm above the breast support table, on top of the homogeneous 0.5 mm Al phantom for the P beams and on top of 20 mm PMMA for the PS beams. The contrast was calculated as the signal difference (ΔP_{out} in equation (20)) between pixel value in the small square of aluminium and the background pixel values in linearized images, determined from a 2 $\times$ 2 mm^2 ROI at the centre of the aluminium and four identical ROIs on the four sides of the aluminium square. SDNR was calculated as the contrast divided by the average standard deviation of pixel values of the four background ROIs.

3.7. Contrast detail measurements using CDMAM

The CDMAM test object was imaged at 29 kV, W/Rh with the mAs settings determined as described in section 3.2. Eight images of the CDMAM were acquired for each beam and grid condition (section 3.2). The CDMAM images were scored using the CDCOM module and c-d curves were generated using the standard processing method described by Young *et al* (2006). Uncertainty on the threshold gold thickness was estimated using a bootstrap method.

3.8. Scatter fraction in the image (SF*out*)

The scatter fractions in the output image (SF_{out}) were measured for the four PS beams with grid out.

3.8.1. Beam stop method. The scatter fractions in the output image (SF_{out}) were determined experimentally with the beam stop method (Carton *et al* 2009, Salvagnini *et al* 2012). A series of lead discs with radii R between 3 and 10 mm were imaged on top of the PMMA, at the centre of the plate, followed by an image without a lead disc. The mean pixel value PV_Q (linearized pixel values) in a circular ROI (2 mm in diameter) positioned on each image at the disc centre gave the scatter and glare (scattering of signal within the detector), noted $PV_Q^{disc} = S_{out} + G_S$, as a function of the disc radius. The mean PV_Q at the same location but without disc gave the primary, scatter and glare: $PV_Q = P_{out} + S_{out} + G_{P+S}$. With the reasonable assumption that glare is proportional to signal, i.e. $G_S = \gamma S_{out}$ and $G_{P+S} = \gamma (P_{out} + S_{out})$, SF_{out} was calculated with equation (24):

$$SF_{out} = \frac{S_{out} + G_S}{P_{out} + S_{out} + G_{P+S}} = \frac{S_{out}}{P_{out} + S_{out}} = \frac{\lim_{R \to 0} PV_Q^{disc}(R)}{PV_Q} \tag{24}$$

The numerator in equation (24) was obtained by extrapolating $PV_Q^{disc}(R)$ plotted as a function of the disc radius to the radius zero. Linear or logarithmic functions are usually used for extrapolation (Aslund *et al* 2006, Shen *et al* 2006, Carton *et al* 2009, Salvagnini *et al* 2012). In our study a fitting function derived from the beam PSF given in equation (1) was used (equation (25)), with the constraints $\lim_{R \to 0} PV_Q^{disc}(R) = S_{out} + G_S$ and $\lim_{R \to \infty} PV_Q^{disc}(R) = 0$:

$$PV_Q^{disc}(R) = DAK \cdot \int_0^{2\pi} \int_R^{\infty} PSF_b(r) r \, dr d\theta$$
$$= \frac{S_{out} + G_S}{ak_1^2 + (1-a)k_2^2} \cdot \left(\frac{ak_1^2}{\left(1 + (R/k_1)^2\right)^{1/2}} + \frac{(1-a)k_2^2}{\left(1 + (R/k_2)^2\right)^{1/2}} \right) \tag{25}$$

*3.8.2. Low-frequency drop of MTF*sys. In a second experimental approach, SF_{out} can be obtained from a measurement of MTF_{sys} (Salvagnini *et al* 2012). The MTF_{sys} in the presence of scattered radiation was measured as described in section 3.4. In the approximation of low glare, MTF_{sys} drop at low spatial frequencies gives $(1 - SF_{out})$ which in turn gives SF_{out} (equation (3*a*)).

3.8.3. Monte Carlo simulation. Finally, an additional estimation of SF_{out} for the PS beams (grid out) was made using a Monte Carlo (MC) technique by means of PENELOPE/penEasy software (Salvat *et al* 2006, Sempau *et al* 2011). In the simulations the source was implemented as a point-like source, constrained within an aperture. The energy distribution of the source was generated via the Boone model (Boone *et al* 1997) and loaded from an external

file. X-ray photons were transported through the geometry and scored in the detector volume using the pixelated imaging detector (PID) tally. A detector pixel size of 5×5 mm was used and the detection mode was set to energy integrating, i.e. the image corresponds to the energy deposited per unit area and per simulated history. The detector itself was implemented as an a-Se layer of thickness 250 μm and dimensions 240×300 mm^2, and the breast table top was simulated as a 1 mm thick carbon fibre layer. The tally can filter the photons arriving at the detector according to the interactions suffered during their trajectory, hence four distinct images could be generated: a primary image (un-scattered photons), a Rayleigh image (photons underwent one Rayleigh scattering event), a Compton image (one Compton scattering event) and a multi-scatter image (photons that had undergone more than one scattering event). The three scatter images were then summed to generate a total scatter image, which was then used together with the primary image to form the scatter fraction image. The scatter fraction was estimated using a 10×10 mm ROI positioned at the centre of the PMMA in the SF image. A run was terminated when the statistical uncertainty in the energy deposition reported by the simulation was less than 0.1%.

3.9. Grid transmissions and beams components

Grid transmissions and beam components were calculated from images with linearized pixel values (PV_Q). The total (T_t) and primary (T_p) grid transmissions were determined for the four P beams from images of circular pinholes of different diameters. A series of circular lead collimators with radii R between 2 and 10 mm were fixed at the tube exit and imaged at a fixed mAs, followed by an image without a collimator. This procedure was repeated with the grid in place and with the grid removed. With the same circular ROI and calculation assumptions as those used for the beam stop method described in section 3.8.1, T_t and T_p were calculated with equations (26a) and (26b), respectively:

$$T_t = \frac{P_{out} + S_{out}}{P_{in} + S_{in}} = \frac{{}^+PV_Q}{{}^-PV_Q} \tag{26a}$$

$$T_p = \frac{P_{out}}{P_{in}} = \lim_{R \to 0} \frac{{}^+PV_Q^{ph}(R)}{{}^-PV_Q^{ph}(R)} \tag{26b}$$

The mean pixel values measured without a pinhole (PV_Q) were used in equation (26a). The plus and minus signs indicate the grid position, i.e. in place and removed. Equation (26b) was evaluated by extrapolating the mean pixel values $PV_Q^{ph}(R)$ measured in a circular ROI (2 mm in diameter) positioned on each image at the pinhole centre and plotted as a function of the pinhole radius to the radius zero. A fitting function derived from the beam PSF given in equation (1) was used (equation (27)), with the constraints $\lim_{R \to 0} PV_Q^{ph}(R) = P_{out} + G_P$ and $\lim_{R \to \infty} PV_Q^{ph}(R) = P_{out} + G_P + S_{out} + G_S$:

$$
\begin{aligned}
PV_Q^{ph}(R) &= DAK \cdot \int_0^{2\pi} \int_0^R PSF_b(r) r \, dr \, d\theta \\
&= P_{out} + G_P + \frac{S_{out} + G_S}{a k_1^2 + (1-a) k_2^2} \cdot \left(a k_1^2 \cdot \left(1 - \frac{1}{\left(1 + (R/k_1)^2\right)^{1/2}} \right) + (1-a) k_2^2 \cdot \left(1 - \frac{1}{\left(1 + (R/k_2)^2\right)^{1/2}} \right) \right)
\end{aligned}
\tag{27}
$$

The differences between the primary grid transmissions measured for the four PS and corresponding P beams were below 2%, thus average values were used for T_p. The PS beam

Table 3. Determination of the x-ray beam components.

Beam type	Grid	P_{out}	S_{out}	P_{in}	S_{in}	SF_{out}	SF_{in}
PS	Out	$(1-SF_{out})\cdot DAK$	$SF_{out}\cdot DAK$	P_{out}	S_{out}	Measured (beam stop)	SF_{out}
PS	In	$P_{in}\cdot T_p$	$DAK - P_{in}\cdot T_p$	Known (=PS grid out)	Known (=PS grid out)	$\frac{DAK-P_{in}\cdot T_p}{DAK}$	Known (=PS grid out)
P	In	$\frac{T_p}{T_t}\cdot\frac{T_t-T_s}{T_p-T_s}\cdot DAK$	$\frac{T_s}{T_t}\cdot\frac{T_p-T_t}{T_p-T_s}\cdot DAK$	$\frac{T_t-T_s}{T_t(T_p-T_s)}\cdot DAK$	$\frac{T_p-T_t}{T_t(T_p-T_s)}\cdot DAK$	$\frac{T_s}{T_t}\cdot\frac{T_p-T_t}{T_p-T_s}$	$\frac{T_p-T_t}{T_p-T_s}$

components were then calculated as shown in table 3, using DAK, T_p and T_t. The scatter grid transmissions (T_s) were calculated with equation (11*b*), using the calculated values S_{out} and S_{in}, and assumed the same for the corresponding P beams (very close HVLs). The parameters for the P beams were finally calculated with DAK, T_p, T_t and T_s, as shown in table 3.

### 3.10. Calculation of DQE*sys*, eDQE and gDQE

All DQE metrics start from the detector DQE (DQE$_d$) (equation (16)). DQE$_{sys}$ was calculated from equation (17), using T_p and T_t. The eDQE was calculated via equation (18*a*) using T_p and SF$_{out}$; this is a different approach to computing eDQE compared to that of Samei *et al* (2009), which involves the measurement of the primary beam transmission through the phantom to estimate P_{in}. The gDQE was calculated using equation (19*a*). Finally, NEQ was calculated using equation (10).

4. Results and discussion

4.1. Scatter fraction in the image (SF*out*) and grid characterization

The calculated beam parameters are given in table 5. The DAK for a constant image noise (target standard deviation of pixel values σ_T) decreases as beam energy increases. This is consistent with results of an earlier study (Marshall 2009) and is partly a result of the increase in detector gain with mean photon energy. Although not shown, the S_{out}/P_{out} ratios increase linearly with the PMMA thickness, as expected (Boone *et al* 2000). With differences below 3%, SF$_{out}$ measured with the beam stop technique (illustration in figure 4 for the Selenia Dimensions, data in table 4) and average SF$_{out}$ calculated from Monte Carlo (MC) simulations for the PS beams with grid out are in good agreement. Agreement was slightly poorer using the low-frequency drop of MTF$_{sys}$ where an underestimate of SF$_{out}$ compared to the two other methods was seen, ranging from -6% (20 mm PMMA) to -10% (70 mm PMMA). In using MTF$_{sys}$ to estimate SF$_{out}$, the hypotheses of signal and SF$_{out}$ stationarity within the different ROIs have to be made and this is not perfectly met in practice. The MC data showed that SF$_{out}$ decreases from image centre to edge and that average SF$_{out}$ is lower than the central value by 6–8%.

The primary grid transmission (T_p), which varied between 0.75 and 0.77 for the two systems, increases with the beam energy whereas the total grid transmission (T_t) for PS beams falls from 0.60 to 0.43 with increasing SF$_{in}$ (table 5), consistent with previous work (Rezentes *et al* 1999, Carton *et al* 2009, Salvagnini *et al* 2012). The T_s values measured in this study are within the range expected for mammography grids (Shen *et al* 2006, Aichinger *et al* 2012, p 126). The utility of the grid is given by the grid DQE (DQE$_{ASD}$ in equation (15*a*) and table 5), which increases with SF$_{in}$, T_p and the grid selectivity ($\Sigma = T_p/T_s$). DQE$_{ASD}$ grows
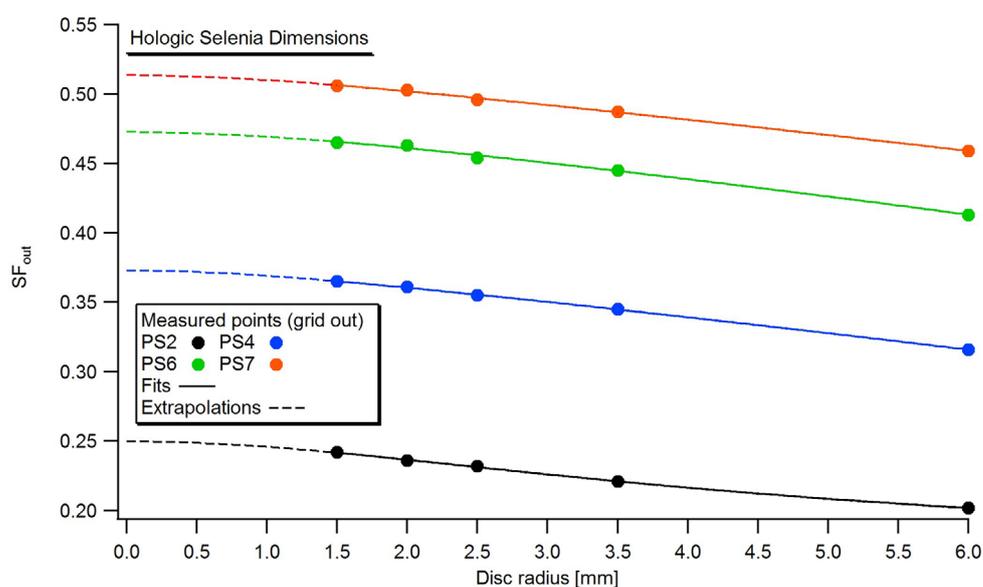
Figure 4. SF_{out} obtained with the beam stop technique for the PS beams with grid out (data: Hologic Selenia Dimensions).

Table 4. Average SF_{out} for PS beams without grid calculated with Monte Carlo simulations and measured with the beam stop technique and the low-frequency drop of MTF_{sys}.

Beam	MC simulation	Beam stop		$MTF_{sys}(0)$	
		Hologic	Siemens	Hologic	Siemens
PS2	0.25	0.247	0.258	0.235	0.240
PS4	0.37	0.371	0.382	0.345	0.358
PS6	0.48	0.472	0.477	0.430	0.440
PS7	0.51	0.511	0.515	0.468	0.470

with SF_{in} from T_p ($SF_{in} = 0$) to $T_p \cdot \Sigma$ ($SF_{in} = 1$). DQE_{ASD} is mainly determined by T_p for low SF_{in}, and is increasingly weighted by the grid selectivity as SF_{in} increases. The cellular grid of the Selenia has a higher selectivity than the classical linear grid of the Siemens, and hence a DQE_{ASD} increasing faster with SF_{in} (figure 5). In mammography, SF_{in} typically lies between 0.2 and 0.5 and consequently the higher selectivity of the cellular grid is of limited value in terms of DQE_{ASD}.

DQE_{ASD} becomes greater than 1.0 for $SF_{in} \geqslant 0.29$ and $\geqslant 0.31$ for the Hologic and Siemens, respectively, corresponding to 50% glandular breast thicknesses of ~38 mm and ~42 mm (Boone *et al* 2000), as shown in figure 5. For lower SF_{in}, the benefit of scatter rejection does not compensate sufficiently for the loss in primary photons; only a grid with $T_p = 1$ improves SNR for all thicknesses. For the conditions used in this study, the grids of the Hologic and Siemens only improve SNR for breasts thicker than 38 and 42 mm, respectively, and hence should be removed below. This outcome in terms of DQE_{ASD} is consistent with K_{SDNR} results ($K_{SDNR} = \sqrt{DQE_{ASD}} = T_p/\sqrt{T_t}$) in previous studies (Chakraborty 1999, Veldkamp *et al* 2003, Shen *et al* 2006). Cunha *et al* (2010) showed K_{SDNR} becomes greater than 1.0 for breasts thicker than 3 cm for grids used at 28 kV (Mo/Mo), while Carton *et al* (2009) measured a

Table 5. Beams and grid characteristics measured for the Hologic and Siemens systems.

Beam	In/Out	T_t	T_p	T_s	DQE_{ASD}	SF_{out}	DAK (μGy)	P_{out} (μGy)	S_{out} (μGy)	P_{in} (μGy)	S_{in} (μGy)
Hologic Selenia Dimensions											
P2	In	0.731	0.759	0.099	0.788	0.006	137.3	136.5	0.8	179.8	8.0
P4	In	0.734	0.760	0.118	0.787	0.007	119.5	118.7	0.8	156.3	6.6
P6	In	0.741	0.765	0.117	0.790	0.006	108.8	108.1	0.6	141.4	5.4
P7	In	0.742	0.769	0.111	0.797	0.006	94.5	93.9	0.6	122.1	5.2
PS2	Out	1.000	1.000	1.000	1.000	0.247	118.2	89.0	29.2	89.0	29.2
PS4	Out	1.000	1.000	1.000	1.000	0.371	109.2	68.7	40.2	68.7	40.5
PS6	Out	1.000	1.000	1.000	1.000	0.472	102.3	54.0	48.3	54.0	48.3
PS7	Out	1.000	1.000	1.000	1.000	0.511	93.4	45.7	47.7	45.7	47.7
PS2	In	0.596	0.759	0.099	0.967	0.041	68.2	65.4	2.8	89.0	29.2
PS4	In	0.522	0.760	0.118	1.107	0.084	55.0	50.4	4.6	68.7	40.5
PS6	In	0.459	0.765	0.117	1.275	0.120	46.6	41.0	5.6	54.0	48.3
PS7	In	0.433	0.769	0.111	1.366	0.132	41.1	35.7	5.4	45.7	47.7
Siemens Inspiration											
P2	In	0.724	0.759	0.166	0.796	0.014	114.8	113.2	1.6	149.2	9.4
P4	In	0.731	0.751	0.180	0.772	0.009	103.4	102.5	0.9	136.5	5.0
P6	In	0.727	0.757	0.183	0.788	0.013	93.8	92.6	1.2	122.3	6.7
P7	In	0.727	0.750	0.187	0.774	0.011	78.6	77.7	0.8	103.7	4.4
PS2	Out	1.000	1.000	1.000	1.000	0.258	117.1	86.9	30.2	86.9	30.2
PS4	Out	1.000	1.000	1.000	1.000	0.382	106.7	65.9	40.8	65.9	40.8
PS6	Out	1.000	1.000	1.000	1.000	0.477	91.7	48.0	43.7	48.0	43.7
PS7	Out	1.000	1.000	1.000	1.000	0.515	87.0	42.2	44.8	42.2	44.8
PS2	In	0.606	0.759	0.166	0.951	0.071	71.1	66.1	5.0	86.9	30.2
PS4	In	0.533	0.751	0.180	1.058	0.129	57.3	49.9	7.4	65.9	40.8
PS6	In	0.483	0.757	0.183	1.186	0.180	44.5	36.5	8.0	48.0	43.7
PS7	In	0.460	0.750	0.187	1.223	0.209	40.3	31.9	8.4	42.2	44.8

SDNR improvement for S_{out}/P_{out} ratios higher than 0.4 for 35 kV (Rh/Rh), that corresponds approximately to $SF_{in} = 0.29$, both close to our results. More recently, Chen *et al* (2015) similarly showed that grid-less imaging in digital mammography gave higher SDNR for PMMAs thinner than 4 cm. Gennaro *et al* (2007) determined a grid break-even at 6.5 cm PMMA (32 kV—Rh/Rh), a thickness much higher than determined in our study. The characteristics of the grid were however not given and the origin of the difference is therefore difficult to establish (most probably due to a lower T_p). It is interesting to note that the grid modifies the SDNR by the factor $T_p/\sqrt{T_t}$ without any change in patient dose. The AEC of most radiology systems will however keep the DAK constant and increase the patient dose by $1/T_t$, changing SDNR by a factor T_p/T_t.

A scan-slot system was not tested in our study but we can estimate a theoretical DQE_{ASD} from scatter rejection data published for the Philips MicroDose multi-slit system (Aslund *et al* 2006). For this system $T_p = 1$ because the slit width (0.7 mm) of the post-collimator is wider than the input primary beam. An approximate value $T_s \approx 0.04$ was used, which is close to the value of 0.03 reported in older studies for multi-slit mammography systems (Yester *et al* 1981, Barnes *et al* 1993), and corresponds to the SDQE ≈ 0.96 given in Aslund *et al* (2006). High primary transmission and excellent scatter rejection hence give a DQE_{ASD} close to that for an ideal ASD (figure 5).
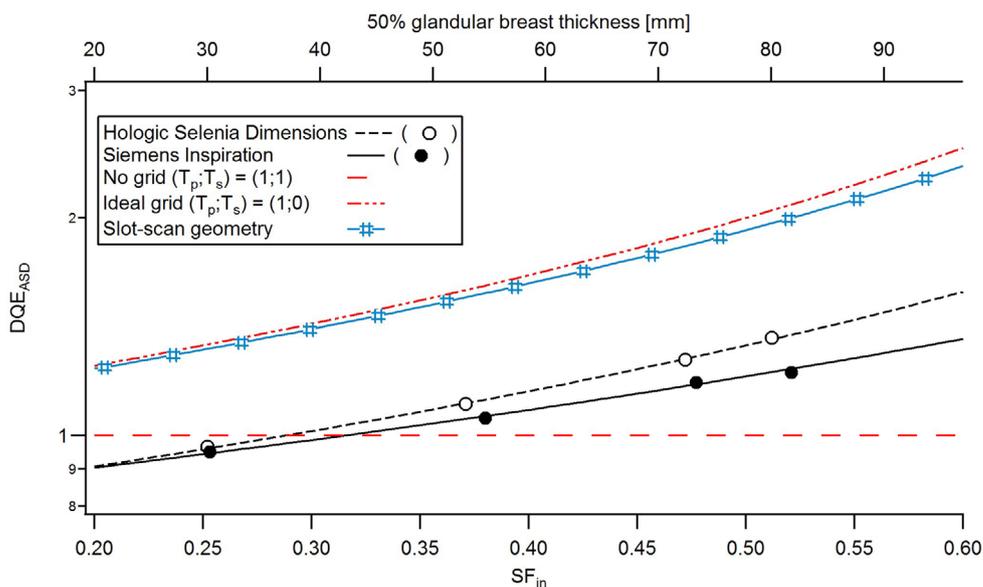
Figure 5. DQE$_{ASD}$ as functions of SF$_{in}$ (measured points and theoretical curves). The 50% glandular breast thickness corresponding to SF$_{in}$ in Boone data (Boone *et al* 2000) is reported in the upper axis.

4.2. System MTF

Figure 6 plots the presampling MTF curves (simply denoted MTF in our study) measured without scatter but including focus and detector blurring. Also plotted are measured MTFs$_{sys}$ (presampling MTFs measured in the presence of scattered radiation), along with the MTF$_{sys}$ determined from equation (3*a*). It can be seen that calculated MTFs$_{sys}$ closely matches measured MTFs$_{sys}$, an indication that cascading the individual transfer functions of the separate processes is a valid step. This in turn, is consistent with the linear transfer of independent and uncorrelated physical processes, as described by Kyprianou *et al* (2004, 2005a) who multiplied the linear combination of the scatter MTF (MTF$_S$), focus MTF (MTF$_F$) and detector presampling MTF (MTF$_D$). MTF$_{sys}$ incorporates these three effects of signal blurring. This result supports the derivation of the system transfer function as the product of the presampling MTF and the BTF (convolution of the impulse responses (PSFs) of the different sources of image degradation). The FWHM of scatter PSFs ranged between 4.9 mm (beam PS2) and 6.4 mm (beam PS7) for the four PS beams with grid out (figure 2), suggesting considerable low spatial frequency content in wide-angle scattering. Furthermore this is evidence that the BTF drops at very low frequency to a value $(1 - SF_{out})$, and can be practically considered as a constant equal to $(1 - SF_{out})$ for spatial frequencies higher than $1/k \approx 0.1 \, \text{mm}^{-1}$ (equation (3*b*)), the frequency range useful for radiology.

Two methods are thus available when determining MTF$_{sys}$. A direct measure can be made, using a large, knife-edge embedded in PMMA, as described by Salvagnini *et al* (2012). MTF$_{sys}$ is however difficult to assess precisely for a number of reasons. First, the sharp edge must be large enough to enable an accurate estimate of the long LSF tails of the wide-angle scatter distribution. Truncation of the LSF tails within a finite ROI causes a spectral truncation at very low spatial frequency. This incorrectly inflates the MTF at all spatial frequencies (Illers *et al* 2005, Samei *et al* 2006, Friedman and Cunningham 2008). Secondly, the value of SF$_{out}$
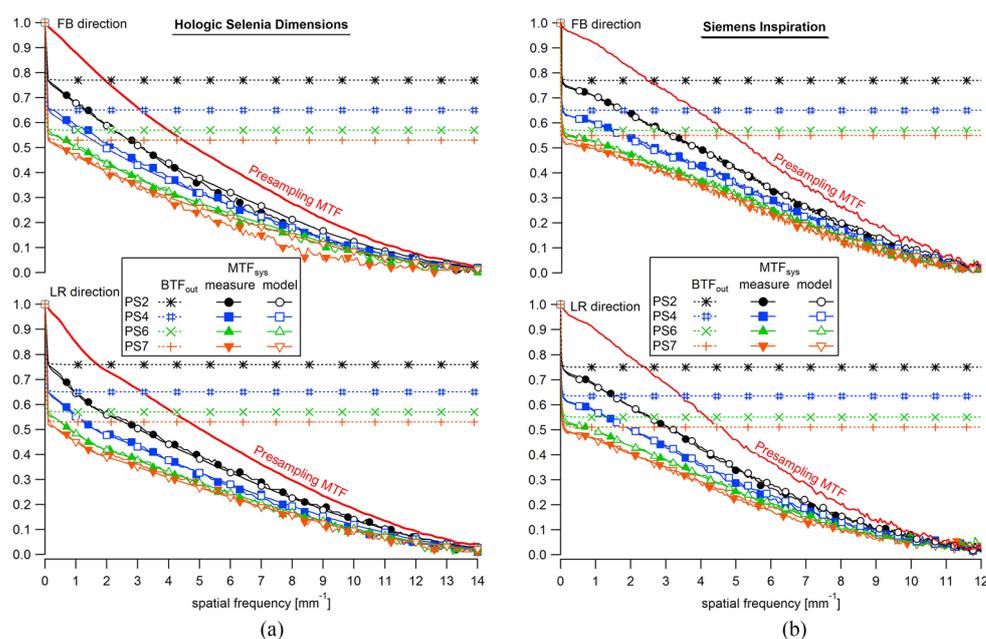
Figure 6. Presampling MTF, BTF$_{out}$ and MTF$_{sys}$ in the left-right (LR) and front-back (FB) directions (a) Hologic Selenia Dimensions (b) Siemens Inspiration.

obtained from MTF$_{sys}$ contains the contribution of glare. The glare fraction in the image can be estimated from the low-frequency drop of the presampling MTF, and then subtracted from the measured low-frequency drop of MTF$_{sys}$ to obtain SF$_{out}$ (Salvagnini *et al* 2012). Thirdly, the calculation of MTF$_{sys}$ assumes the spatial stationarity of the detector and beam PSFs. Wide-angle scattering within the finite size of the x-ray field results in a slowly varying SF$_{out}$ across the image plane. The assumption of spatial stationarity is thus not fully met and this will somewhat decrease the precision of the MTF$_{sys}$ low-frequency drop estimate.

The alternative is to perform separate measures of the presampling MTF (without scatter) and of SF$_{out}$, typically using a beam stop method. The beam stop method gives a direct and local measure of SF$_{out}$, and is therefore expected to give a more accurate estimate of low-frequency drop. This also quantifies the spatial spread of the scatter PSF (factors k_1 and k_2 in equation (1)). In this work, average SF$_{out}$ in the PMMA calculated from Monte Carlo simulations and by beam blocks were consistent, whereas the low-frequency drop of MTF$_{sys}$ underestimates SF$_{out}$ by ~6%. This may be partially explained by differences in SF$_{out}$ between the centre and the edge of the ROI used to compute MTF$_{sys}$. The assumptions of spatial invariance are not fully met. A small contribution to the difference may also come from the scattered radiation originating from the edge device that tends to inflate the MTF (Neitzel *et al* 2004), and hence can reduce the low-frequency drop.

4.3. Image quality and detection: NEQ and contrast-detail analysis

Pairwise comparison of NEQs between equivalent beams without and with scatter (P beams versus PS beams without grid) shows that NEQ varies proportionally to $(1 - SF_{out})^2$ for a constant image noise (equation (10) and figure 7). The PS beams with grid have the same mAs
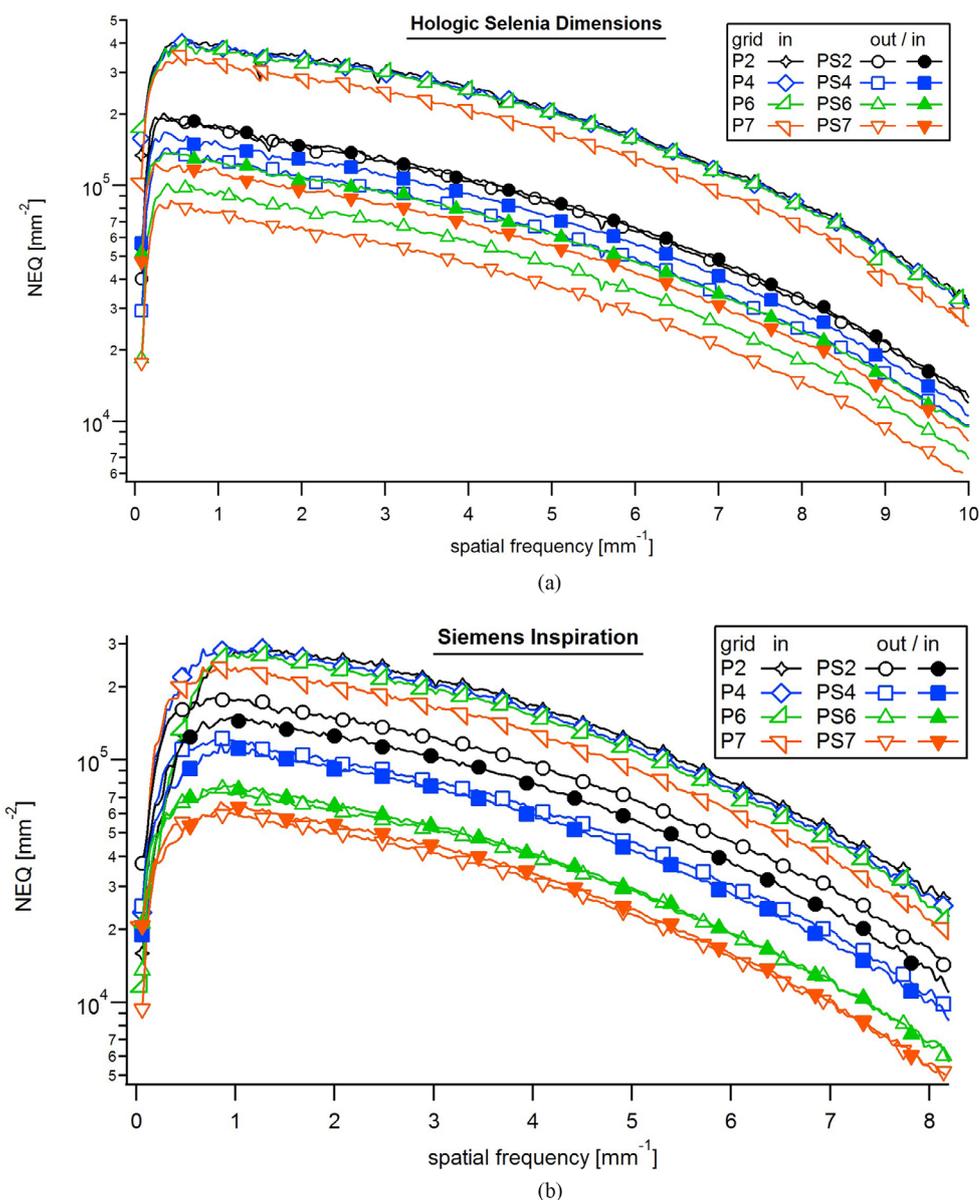
Figure 7. NEQ (a) Hologic Selenia Dimensions (b) Siemens Inspiration.

and SF_{in} as the corresponding PS beams without grid, but reduced DAK and SF_{out}. In terms of NEQ, P_{out}^2 is reduced by the primary grid transmission (T_p^2) whereas the NPS varies with the total grid transmission (T_t). Hence, the variation in NEQ due to the grid follows the ratio T_p^2/T_t, i.e. an increase or a decrease if DQE_{ASD} is greater or less than 1.0. The grid is seen to improve the NEQ for the beams PS6 and PS7, slightly for PS4, but decreases the NEQ for PS2.

The contrast of the 0.2 mm aluminium foil measured on the images (ΔP_{out}) was normalized by the product $\mu_{Al}T$, where μ_{Al} is the attenuation coefficient of aluminium given in table 2 and $T = 0.2$ mm. The values $\Delta P_{out}/(\mu_{Al}T)$ were then compared to primary DAK in the image
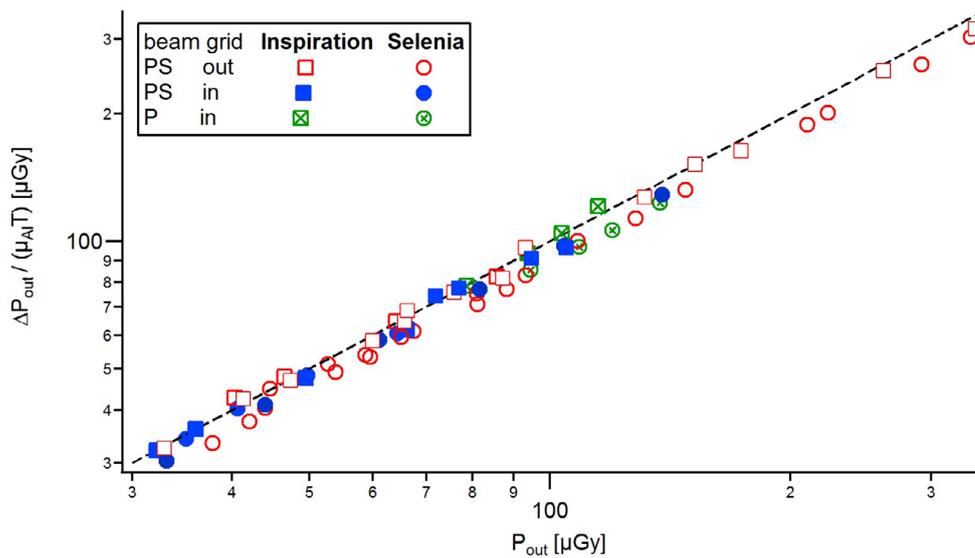
Figure 8. Contrast of a 0.2 mm aluminium foil measured on the images and normalized by the product $\mu_{Al}T$ compared to P_{out} determined by beam stop for different scatter conditions. The dotted line shows the theoretical relationship (identity function).

(P_{out}) (figure 8). Good equivalence between $\Delta P_{out}/(\mu_{Al}T)$ and P_{out} is seen, consistent with the expectation that object contrast is made of primary photons only (equation (20)), regardless the number of scattered photons in the image, whereas the noise increases with the total number of detected photons, without distinction between primary and scatter. Hence, as shown in figure 8, working at constant number of photons at the detector (typical of an AEC) will give a constant quantum noise but will not ensure a constant contrast or SDNR, both varying with $(1 - SF_{out})$ (equation (21)). The factor $(1 - SF_{out})^2$ represents the degree to which increased DAK can be used to compensate the SDNR for x-ray scatter degradation. This was shown by Siewerdsen and Jaffray (2000), and has been verified in a recent study into AEC set-up for a mammography system (Salvagnini *et al* 2015).

Turning to the CDMAM data, figures 9(a) and (b) present the c-d curves for the Hologic and Siemens systems, respectively. The threshold gold thickness (T) in the upper graph in each figure reveals the negative influence of increasing SF_{out} on detection. Equations (23a) and (23b) predict the value $P_{out}\mu_{Au}T/\sigma$ will remain constant (μ_{Au} values in table 2). Considering $P_{out}\mu_{Au}T/\sigma$ instead of T alone in the c-d curves cancels the differences in detectability levels (lower graphs in figures 9(a) and (b)). The pairwise variations of threshold thicknesses between equivalent beams without and with scatter (P beams versus PS beams without grid) show that T is systematically increased by $(1 - SF_{out})^{-1}$ (at constant noise σ_T) compared to the conditions without scatter. This result validates the link between MTF and MTF$_{sys}$ of equation (4) that shows the signal scales with the number of primary photons (for frequencies higher than $1/k$), whereas the noise increases with the total amount of photons. The SF in the output image (SF$_{out}$) reduces the NEQ by $(1 - SF_{out})^2$ and increases T by $(1 - SF_{out})^{-1}$, that can be offset by an increase in DAK of $(1 - SF_{out})^{-2}$, called 'scatter compensation factor' in Siewerdsen and Jaffray (2000).

The experimental variations in T with SF_{out} behave as predicted by the NPWE observer, that makes use of the image noise (composed of primary and scattered photons without
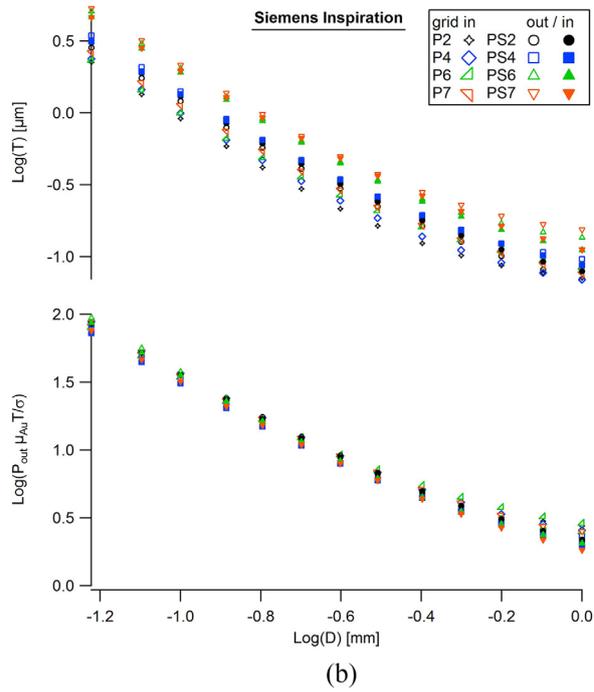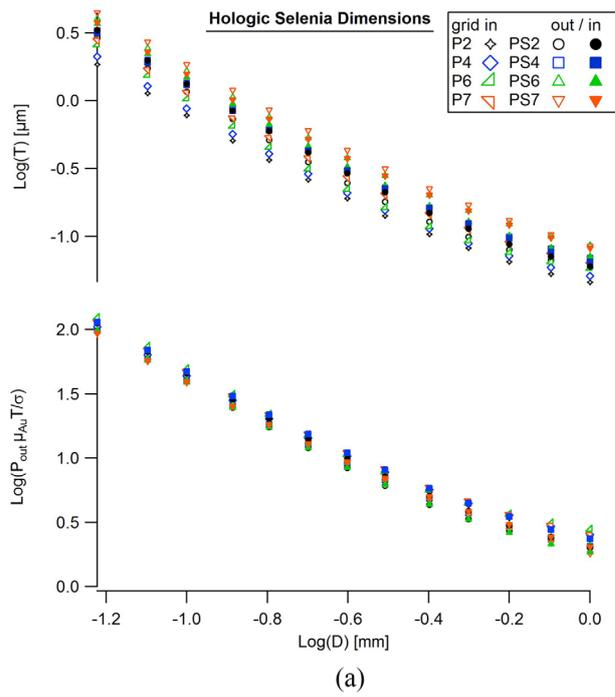
Figure 9. Contrast-detail curves of the CDMAM as functions of log(*D*). (a) Hologic Selenia Dimensions (b) Siemens Inspiration. The two upper graphs show raw threshold gold thickness (*T*) data while the two lower graphs show *T* corrected for primary content, energy dependence of gold attenuation coefficient and image noise ($P_{out}\mu_{Au}/\sigma$).
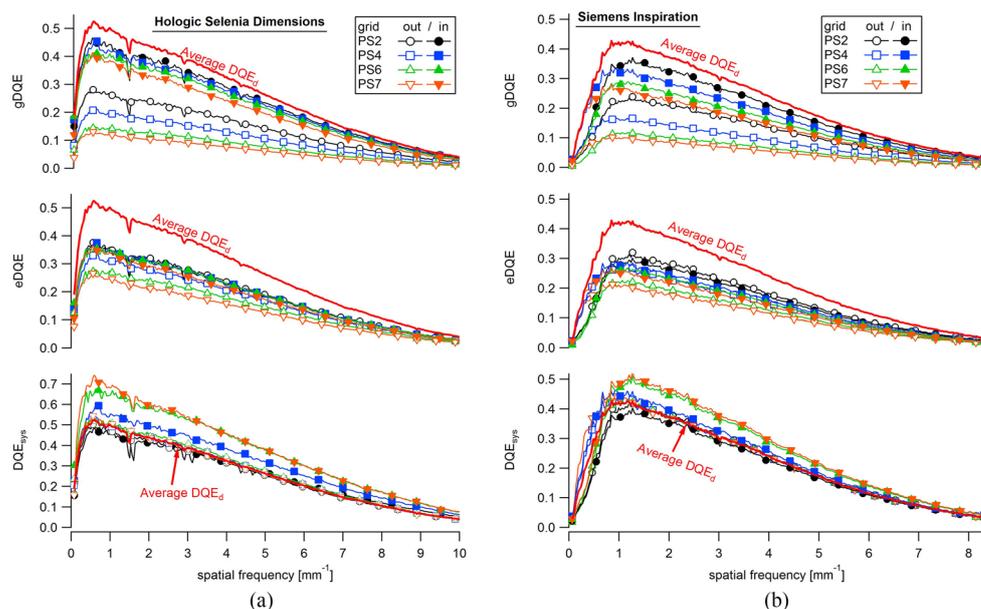
Figure 10. Average DQE_d, eDQE, gDQE and DQE_{sys}. (a) Hologic Selenia Dimensions (b) Siemens Inspiration.

distinction) and the primary object signal (contrast). The NPWE model can thus also be used for image quality characterization with scatter. The effect of scatter in the observer model may be taken into account in two ways: (1) using the presampling MTF (including the detector and focal spot blurs) along to the absolute object contrast (signal difference ΔP_{out}) and NPS (both measured on the images with scatter) (equation (23*a*)) or (2) using the system MTF (MTF_{sys}) along to the normalized object contrast ($\Delta P_{out}/P_{out}$) and NNPS, all three measured with scatter (equation (23*b*)). Both methods have been used in the literature: Monnin *et al* (2011) used the presampling MTF, while Liu *et al* (2014) used generalized MTF and NNPS in their observer model. The latter study showed the equivalence of the two approaches.

4.4. From detector DQE to system DQE

Figures 10(a) and (b) plot DQE_{sys}, the average detector DQE (IEC 2015), eDQE (Samei *et al* 2009) and gDQE (Kyprianou *et al* 2004, 2005a, for the Selenia Dimensions and Inspiration, respectively. All the images were made with the detector carbon cover in place, and all these detection efficiency metrics—even the detector DQE—include the loss in detection efficiency due to x-ray absorption within the detector cover. Although not shown, maximum variation in the individual DQE curves for a given detector for the P beams was 2%, consistent with the beams being designed to have only small changes in effective energy. This small change in detector DQE with energy is consistent with results for an earlier a-Se detector (Marshall 2009) and hence we use an average curve to represent detector DQE.

For the conditions with scatter (PS beams) and grid out, figure 10 shows how eDQE and gDQE decrease with SF_{in}. If no grid is used, DQE_{sys} reverts to DQE_d and is constant, whereas image quality reflected in the NEQ is degraded as SF_{in} increases. The system DQE varies only if there is a change in SNR (NEQ) transfer through the system, but image quality (~NEQ) can vary independently because of variations in the quantity of input primary photons (SF_{in}).

Without the grid, the only element in the imaging system is the detector: if detector DQE is ~constant (energy is kept ~constant) then a change in system efficiency is not expected. The system DQE cascades detector and ASD DQEs, and quantifies SNR changes as an output/input balance for the whole imaging system (detector + ASD). It differs from detector DQE only when an ASD is used, and is therefore a parameter suitable for the imaging efficiency assessment of a detector/ASD pair, as a function of SF_{in}. The eDQE compares the real system to a perfect detector with a perfect grid ($DQE_d = 1$ and $SF_{out} = 0$), and scales as $(1 - SF_{in})$ for the case without grid. The gDQE scales as $(1 - SF_{out})^2$, as does NEQ. When imaging without grid, the ability of the imaging system to select primary photons or reject scattered photons does not vary between the different beams and hence we expect no change in system efficiency, yet eDQE and gDQE decrease with increasing PMMA thickness implying a reduction in system efficiency. This result suggests that eDQE and gDQE are mixing image quality and system efficiency. This property comes from the use of a grid DQE as defined by Wagner *et al* (1980) and implicitly taken up for eDQE and gDQE that ranks the real grid to an ideal device with $(T_p; T_s) = (1; 0)$. As a consequence, both eDQE and gDQE, for detectors coupled to real ASDs, behave as if the grid were the source of the scatter incident on the detector and can therefore only be lower than the detector DQE (for real grids) or equal to the detector DQE for the case of an ideal grid. We suggest that metrics of system efficiency and metrics of image quality should be kept separate. 'Image quality' can then be defined and calculated separately, for example using a detectability index for some task in combination with the NEQ (Siewerdsen and Jaffray 2000) or even using a task generic parameter such as SDNR.

The introduction of the grid into the system increases DQE_{sys} and eDQE by T_p^2/T_t (the grid DQE), and gDQE by the factor T_p^2/T_t^2. These variations can be tracked for image quality (NEQ with and without grid in figure 7) and for DQE_{sys}, eDQE and gDQE in figure 10. Variations in SNR due to the grid can be basically quantified with SDNR measurements, and related to the dose (mAs) for a given beam quality. Figure 11 compares SDNR for a 0.2 mm Al target for grid in and grid out using the four PS beams. The SDNR with grid out was measured for different tube loads (mAs) and compared to the SDNR with grid in with the mAs chosen by the AEC. For the beam PS7, the AEC mAs of the Selenia Dimensions was above the maximum allowed for 29 kV—W/Rh and thus 400 mAs (i.e. maximum) was chosen. As expected from equation (21), the SDNR increases as a power function of the DAK and hence of mAs for fixed x-ray beam and phantom. SDNR therefore scales with $(1 - SF_{out})$ i.e. decreases with the PMMA thickness. For a given mAs, the grid improves the SDNR for the beams PS6 and PS7, but reduces SDNR for the beam PS2, and marginally modifies SDNR for PS4. The introduction of the grid into the system modifies the SDNR by a factor close to the square root of the measured grid DQEs ($T_p/\sqrt{T_t}$) for the different thicknesses (SF_{in}). In our study, DQE_{sys} is higher than the detector DQE for 50% glandular breast thicker than approximately 38 and 42 mm for the Hologic and Siemens, respectively. Below these break-even thicknesses the negative effect of the grid (loss of SDNR due to a loss in primary photons) overcomes the positive effect (increase of SDNR due to rejection of scatter) and degrades the image SDNR.

System DQE considers the imaging system as a cascaded chain of elements. The BTF and presampling MTF are independent, and are multiplied as cascaded processes to describe the signal transfer through the imaging chain. DQE_{sys} is simply the product between the detector and ASD DQEs, where DQE_{ASD} ranks the real SNR^2 transfer through the ASD without considering a hypothetical ideal case. DQE_{sys} reverts to the detector DQE in the absence of an ASD, and will be higher or lower than the detector DQE, depending on how the ASD modifies image SNR. System DQE can be seen as a natural extension of the classical detector DQE and can be used to study the detective efficiency of complete imaging systems for beams with scatter. The newly proposed metric DQE_{sys} is an extension of current detector characterization for imaging systems with
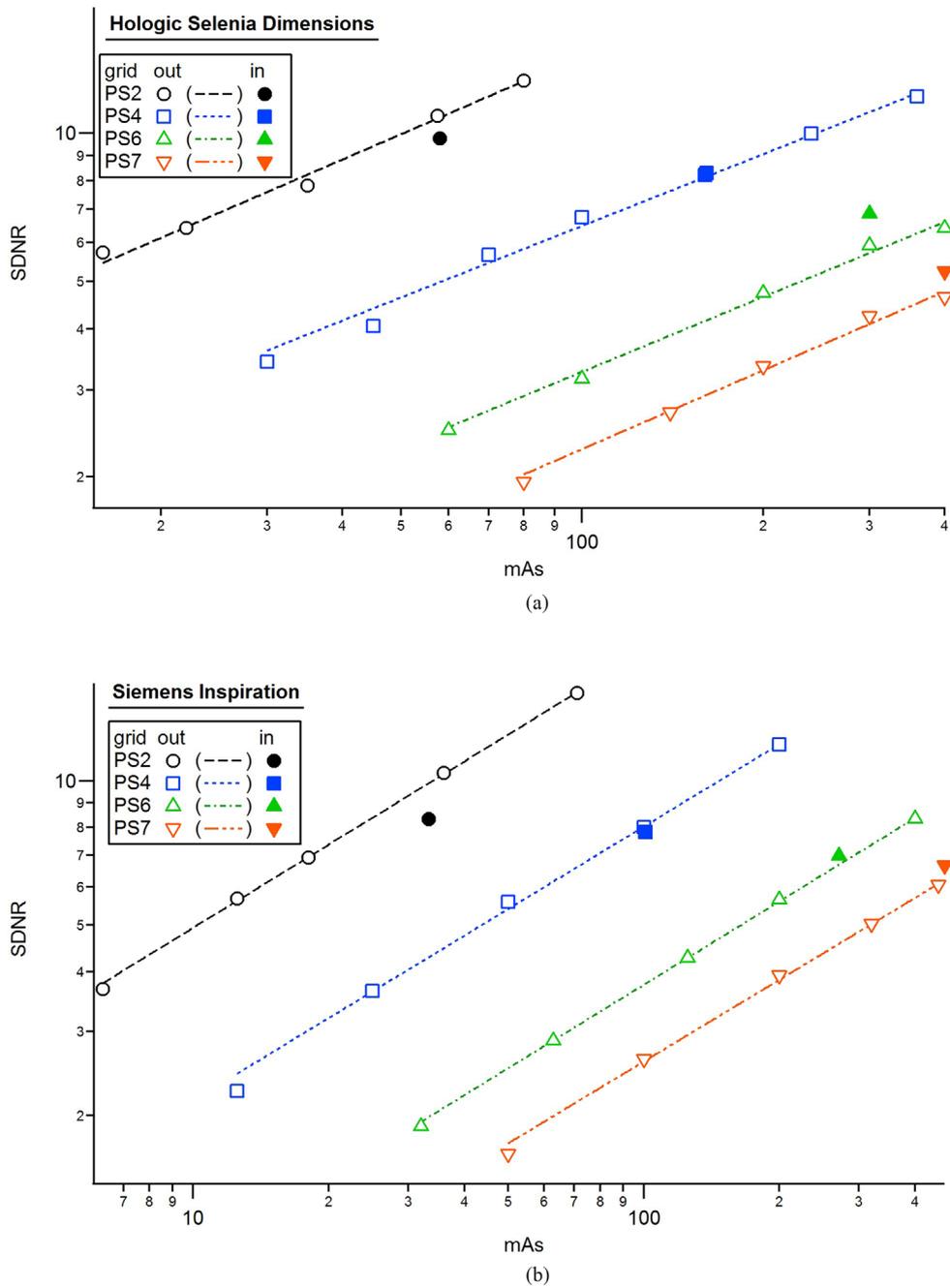
Figure 11. SDNR provided by 0.2 mm Al as a function of mAs for PS beams with and without grid. (a) Hologic Selenia Dimensions (b) Siemens Inspiration.

ASD and beams with scatter. Ideal (primary) and real (primary + scatter) mammography beams were matched in this study using effective energy (HVL) and the assumed equivalence of 10 mm PMMA ~0.5 mm Al. This is similar to the use of Al filters at the tube exit in the IEC recommendations (2015) for detector DQE assessments in order to create a primary beam with the same

effective energy or half value layer (HVL) as typical exit spectra from patients. Characterizing a system using DQE_{sys} could begin with standard (primary beam) detector DQE assessment for the chosen kV and A/F. The additional Al filter thickness at the tube exit should match the HVL of the beam with PMMA. The effect of scatter on image quality (NEQ) and system efficiency (DQE_{sys}) can then be established separately by measuring SF_{out} and DQE_{ASD} for chosen scatter conditions (different SF_{in}). DQE_{ASD} is multiplied by detector DQE to obtain DQE_{sys}. The NEQ and DQE_{sys} assessment can be repeated for different beam energies (different kV and/or A/F) as required. The measurement of MTF_{sys}, which can be a challenge to assess precisely in scatter beams, is not required for NEQ and DQE_{sys}. Just three supplementary variables are needed: the primary and total ASD transmissions and the SF at the detector (SF_{out}). Different methodologies have already been used to quantify SF_{out}, and the beam stop method described in this study gave consistent results. T_t is easily obtained through measurements of signal ratios with grid in/out on linearized images, while an extrapolation of the signal ratio grid in/out to a point source beam was used for T_p measurements. The procedure followed in this study to determine T_p and T_t is however not practicable for slit-scanning systems because the beam components P_{out} and S_{out} are not accessible; an alternative method is proposed in appendix B for such systems.

5. Conclusion

This study has introduced and applied a new methodology for assessing the global performance of projection imaging systems that accounts for scatter and anti-scatter device efficiency in addition to the detector properties and focal sport blur. The following conclusions can be made. Cascaded linear system theory can be used to describe signal degradation and image noise contribution from scatter, including SNR transfer through the scatter reduction device in the form of a specific figure of merit (DQE_{ASD}). The global system efficiency metric (DQE_{sys}) is the product of DQE_{ASD} and the standard DQE of the x-ray detector. The effect of scatter upon the contrast transfer through the system can be described by the convolution of the presampling MTF with the beam (scatter) MTF, equivalent to the low-frequency MTF drop whose amplitude is equal to the scatter fraction in the image. These metrics inserted in the NPWE observer model correctly predicted the object detectability drop due to scatter.

The experimental measurement technique used in this work is proposed as an extension of the current guidance on image quality and detective quantum efficiency for imaging systems with an ASD in the presence of scatter. This involves the determination of the standard detector DQE using a scatter free beam of equivalent energy, and the assessment of the primary and total transmissions of the ASD for the beam with scatter. DQE_{sys} clearly separates system SNR transfer efficiency from estimates of image quality. The result is a simple and robust method for the objective evaluation of both image quality and system efficiency in scatter and is proposed for the characterization of imaging chains.

Acknowledgments

Appendix A. Calculation of $OTF_b(f)$ and $BTF(f)$

The optical beam transfer function (OTF_b) is the Fourier transform of the 2D beam PSF (PSF_b). The radial symmetry of PSF_b leads to a Hankel transform (or Fourier-Bessel transform) of PSF_b (Piessens 2000):

$$\mathrm{OTF_b}\left(f\right) = 2\pi \cdot \int_0^\infty \mathrm{PSF_b}(r)J_0\left(2\pi rf\right)r\mathrm{d}r \tag{A.1}$$

where $J_0(x)$ is the zero order Bessel function of the first kind. The fitting function derived from the beam PSF given in equation (1) gives the following form for $\mathrm{OTF_b}(f)$:

$$\mathrm{OTF_b}\left(f\right)$$

$$= 2\pi \left\{ K_1 \left(1 - \mathrm{SF}\right) \cdot \int_0^\infty \delta(r)J_0\left(2\pi rf\right)\mathrm{d}r + K_2 \cdot \mathrm{SF} \cdot \int_0^\infty \left(\frac{a}{\left(1 + (r/k_1)^2\right)^{3/2}} + \frac{1-a}{\left(1 + (r/k_2)^2\right)^{3/2}} \right) J_0\left(2\pi rf\right)r\mathrm{d}r \right\} \tag{A.2}$$

The integral of the Dirac function is equal to 1.0. The scatter term gives exponential functions.

$$\mathrm{OTF_b}\left(f\right) = 2\pi \left\{ K_1 \cdot \left(1 - \mathrm{SF}\right) + K_2 \cdot \mathrm{SF} \cdot \left(ak_1^2 \exp\left(-2\pi k_1 f\right) + (1-a)k_2^2 \exp\left(-2\pi k_2 f\right)\right) \right\} \tag{A.3}$$

The Fourier transform of an even function is real and $\mathrm{OTF_b}(f)$ is equal to $\mathrm{BTF}(f)$. The normalization of $\mathrm{BTF}(f)$ to 1.0 at zero frequency gives:

$$\begin{cases} K_1 = 1/2\pi \\ K_2 = 1/\left(2\pi \left(ak_1^2 + (1-a)k_2^2\right)\right) \end{cases} \tag{A.4}$$

The expression for $\mathrm{BTF}(f)$ is finally:

$$\mathrm{BTF}\left(f\right) = \left(1 - \mathrm{SF}\right) + \mathrm{SF} \cdot \frac{ak_1^2 \exp\left(-2\pi k_1 f\right) + (1-a)k_2^2 \exp\left(-2\pi k_2 f\right)}{ak_1^2 + (1-a)k_2^2} \tag{A.5}$$

Appendix B. $\mathrm{DQE_{sys}}$ measurement for slit-scanning systems

The procedure followed in this study to calculate $\mathrm{DQE_{sys}}$ is not practicable for slit-scanning systems. The ASD (secondary slit) of these systems is fixed and the $\mathrm{DQE_{ASD}}$ cannot be measured independently. In this case, the beam components P_{out} and S_{out} are not accessible; only the input parameters P_{in} and S_{in} can be measured. The air kerma will be measured at the ASD input for the PS beam ($K_{in}^{PS} = P_{in}^{PS} + S_{in}^{PS}$) and for the equivalent P beam ($K_{in}^{P} = P_{in}^{P}$), using the two tube loads obtained with the AEC. The AEC will give the same DAK ($P_{out}^{PS} + S_{out}^{PS} = P_{out}^{P}$). If the very small SF in fan P beams can be neglected, it gives:

$$T_t = \frac{P_{out}^{PS} + S_{out}^{PS}}{P_{in}^{PS} + S_{in}^{PS}} = \frac{P_{out}^{P}}{K_{in}^{PS}} = \frac{P_{in}^{P}}{K_{in}^{PS}} T_p = \frac{K_{in}^{P}}{K_{in}^{PS}} T_p \tag{B.1}$$

$\mathrm{DQE_{sys}}$ for slit-scanning systems can thus be estimated using the measured K_{in}^{P} and K_{in}^{PS}:

$$\mathrm{DQE_{sys}}\left(f\right) = \left(\frac{T_p}{T_t}\right)^2 \cdot \frac{\mathrm{MTF}^2\left(f\right)}{\mathrm{NNPS}\left(f\right) \cdot \left(\tilde{P}_{out} + \tilde{S}_{out}\right)/T_t} = \left(\frac{K_{in}^{PS}}{K_{in}^{P}}\right)^2 \cdot \frac{\mathrm{MTF}^2\left(f\right)}{\mathrm{NNPS}\left(f\right) \cdot \left(\tilde{P}_{in} + \tilde{S}_{in}\right)} \tag{B.2}$$

References

Aichinger H, Dierker J and Säbel M 2012 *Radiation Exposure and Image Quality in X-Ray Diagnostic Radiology* 2nd edn (Berlin: Springer) p 126

Aslund M, Cederström B, Lundqvist M and Danielsson M 2006 Scatter rejection in multislit digital mammography *Med. Phys.* **33** 933–40

Barnes G T, Wu X and Wagner A 1993 Scanning slit mammography *Med. Prog. Technol.* **19** 7–12

Bertolini M, Nitrosi A, Rivetti S, Lanconelli N, Pattacini P, Ginocchi V and Iori M 2012 A comparison of digital radiography systems in terms of effective detective quantum efficiency *Med. Phys.* **39** 2617–27

Boone J M, Arnold B A and Seibert J A 1986 Characterization of the point spread function and modulation transfer function of scattered radiation using a digital imaging system *Med. Phys.* **13** 254–6

Boone J M and Seibert J A 1997 An accurate method for computer-generating tungsten anode x-ray spectra from 30 to 140 kV *Med. Phys.* **24** 1661–70

Boone J M, Lindfors K K, Cooper V N and Seibert J A 2000 Scatter/primary in mammography: comprehensive results *Med. Phys.* **27** 2408–16

Carton A-K, Vanderbroucke D, Struye L, Maidment D A, Kao Y-H, Albert M, Bosmans H and Marchal G 2005 Validation of MTF measurement for digital mammography control *Med. Phys.* **32** 1684–95

Carton A-K, Acciavatti R, Kuo J and Maidment A D A 2009 The effect of scatter and glare on image quality in contrast-enhanced breast imaging using an a-Si/CsI(Tl) full-field flat panel detector *Med. Phys.* **36** 920–8

Chakraborty D P 1999 The effect of the antiscatter grid on full-field digital mammography images *J. Digit. Imaging* **12** 12–22

Chan H P, Lam K L, Struye L and Wu Y 1990 Studies of performance of antiscatter grids in digital radiography: effect on signal-to-noise ratio *Med. Phys.* **17** 655–64

Chen H, Danielsson M, Xu C and Cederström B 2015 On image quality metrics and the usefulness of grids in digital mammography *J. Med. Imaging* **2** 013510

Cunha D M, Tomal A and Poletti M E 2010 Evaluation of scatter-to-primary ratio, grid performance and normalized average glandular dose in mammography by Monte Carlo simulation including interference and energy broadening effects *Phys. Med. Biol.* **55** 4335–59

Cunningham I A and Shaw R 1999 Signal-to-noise optimization of medical imaging systems *J. Opt. Soc. Am.* A **16** 621–32

Cunningham I A 2000 Applied linear-systems theory *Handbook of Medical Imaging* vol 1, ed J Beutel *et al* (Bellingham, WA: SPIE) pp 79–159

Cunningham I A, Sattarivand M, Hajdok G and Yao J 2004 Can a Fourier-based cascaded-systems analysis describe noise in complex shift-variant spatially sampled detectors? *Proc. SPIE* **5368** 79–88

European Commission 2006 The European protocol for the quality control of the physical and technical aspects of mammography screening: part B. Digital mammography *European Guidelines for Breast Cancer Screening* 4th edn (Luxembourg: European Commission)

Friedman S N and Cunningham I A 2008 Normalization of the modulation transfer function: the open-fild approach *Med. Phys.* **35** 4443–49

Gennaro G, Katz L, Souchay H, Klausz R, Alberelli C and di Maggio C 2007 Grid removal and impact on population dose in full-field digital mammography *Med. Phys.* **34** 547–55

Gopal A and Samant S S 2008 Validity of the line-pair bar-pattern method in the measurement of the modulation transfer function (MTF) in megavoltage imaging *Med. Phys.* **35** 270–9

Hunt D C, Tanioka K and Rowlands J A 2007 X-ray imaging using avalanche multiplication in amorphous selenium: investigation of depth dependent avalanche noise *Med. Phys.* **34** 976–86

IEC (International Electrotechnical Commission) 2015 *Medical Electrical Equipment—Characteristics of Digital X-Ray Imaging Devices—Part 1-1: Determination of the Detective Quantum Efficiency—Detectors used in radiographic imaging IEC 62220-1-1:2015* 1.0 edn (Geneva: IEC)

IEC (International Electrotechnical Commission) 2013 *Diagnostic X-Ray Imaging Equipment—Characteristics of General Purpose and Mammographic Anti-Scatter Grids IEC 60627:2013* 3.0 edn (Geneva: IEC)

Illers H, Buhr E, Günther-Kohfahl S and Neitzel U 2005 Measurement of the modulation transfer function of digital x-ray detectors with an opaque edge-test device *Radiat. Prot. Dosim.* **114** 214–19

Jain A, Kuhls-Gilcrist A T, Gupta S K, Bednarek D R and Rudin S 2010 Generalized two-dimensional (2D) linear system analysis metrics (gMTF, gDQE) for digital radiography systems including the effect of focal spot, magnification, and detector characteristics *Proc. SPIE* **7622** 76220K:1-10

Kim H K 2006 Generalized cascaded model to assess noise transfer in scintillator-based x-ray imaging detectors *Appl. Phys. Lett.* **89** 233504

Kyprianou I S, Rudin S, Bednarek D R and Hoffmann K R 2004 Study of the generalized MTF and DQE for a new microangiographic system *Proc. SPIE Int. Soc. Opt. Eng.* **5368** 349–60

Kyprianou I S, Rudin S, Bednarek D R and Hoffmann K R 2005a Generalizing the MTF and DQE to include x-ray scatter and focal spot unsharpness: application to a new microangiographic system *Med. Phys.* **32** 613–26

Kyprianou I S, Ganguly A, Rudin S, Bednarek D R, Gallas B D and Myers K J 2005b Efficiency of the human observer compared to an ideal observer based on a generalized NEQ which incorporates scatter and geometric unsharpness: evaluation with a 2AFC experiment *Proc. SPIE Int. Soc. Opt. Eng.* **5749** 251–62

Liu H, Chakrabarti K, Kaczmarek R V, Benevides L, Gu S and Kyprianou I S 2014 Evaluation of clinical full field digital mammography with the task specific system-model-based Fourier Hotelling observer (SMFHO) SNR *Med. Phys.* **41** 051907

Marshall N W 2006 A comparison between objective and subjective image quality measurements for a full field digital mammography system *Phys. Med. Biol.* **51** 2441–63

Marshall N W 2009 Detective quantum efficiency measured as a function of energy for two full-field digital mammography systems *Phys. Med. Biol.* **54** 2845–61

Metz C E, Wagner R F, Doi K, Brown D G, Nishikawa R M and Myers K J 1995 Towards consensus on quantitative assessment of medical imaging systems *Med. Phys.* **22** 1057–61

Monnin P, Marshall N W, Bosmans H, Bochud F O and Verdun F R 2011 Image quality assessment in digital mammography: part II. NPWE as a validated alternative for contrast detail analysis *Phys. Med. Biol.* **56** 4221–38

Monnin P, Bosmans H, Verdun F R and Marshall N W 2014 Comparison of the polynomial model against explicit measurements of noise components for different mammography systems *Phys. Med. Biol.* **59** 5741–61

Monnin P, Bosmans H, Verdun F R and Marshall N W 2016 A comprehensive model for quantum noise characterization in digital mammography *Phys. Med. Biol.* **61** 2083–108

Neitzel U 1992 Grids or air gaps for scatter reduction in digital radiography: a model calculation *Med. Phys.* **19** 475–81

Neitzel U, Buhr E, Hilgers G and Granfors P R 2004 Determination of the modulation transfer function using the edge method: influence of scattered radiation *Med. Phys.* **31** 3485–91

Piessens R 2000 The Hankel transform *The Transforms and Applications Handbook* 2nd edn, ed A D Poularikas (Boca Raton, FL: CRC Press)

Rabbani M, Shaw R and Van Metter R 1987 Detective quantum efficiency of imaging systems with amplifying and scattering mechanisms *J. Opt. Soc. Am.* A **4** 895–901

Rezentes P S, de Almeida A and Barnes G T 1999 Mammography grid performance *Radiology* **210** 227–32

Salvagnini E, Bosmans H, Struelens L and Marshall N W 2012 Quantification of scattered radiation in projection mammography: four practical methods compared *Med. Phys.* **39** 3167–80

Salvagnini E, Bosmans H, Struelens L and Marshall N W 2013 Effective detective quantum efficiency for two mammography systems: measurement and comparison against established metrics *Med. Phys.* **40** 101916

Salvagnini E, Bosmans H, Struelens L and Marshall N W 2015 Tailoring automatic exposure control toward constant detectability in digital mammography *Med. Phys.* **42** 3834–47

Salvat F, Fernandez-Varea J M and Sempau J 2006 *Penelope 2006: a Code System for Monte Carlo Simulation of Electron and Proton Transport* (Paris: EOCD Publishing)

Samei E, Flynn M J and Reimann D A 1998 A method for measuring the presampled MTF in digital radiographic systems using an edge test device *Med. Phys.* **25** 102–13

Samei E, Saunders R S, Lo J Y, Dobbins J T, Jesneck J L, Floyd C E and Ravin C E 2004 Fundamental imaging characteristics of a slot-scan digital chest radiography system *Med. Phys.* **31** 2687–98

Samei E, Lo J Y, Yoshizumi T T, Jesneck J L, Dobbins J T, Floyd C E, McAdams H P and Ravin C E 2005 Comparative scatter and dose performance of slot-scan and full-field digital chest radiography systems *Radiology* **235** 940–9

Samei E, Ranger N T, Dobbins J T and Chen Y 2006 Intercomparison of methods for image quality characterization. I. Modulation transfer function *Med. Phys.* **33** 1454–65

Samei E, Ranger N T, MacKenzie A, Honey I D, Dobbins J T and Ravin C E 2009 Effective DQE (eDQE) and speed of digital radiographic systems: an experimental methodology *Med. Phys.* **36** 3806–17

Seibert J A, Nalcioglu O and Roeck W W 1984 Characterization of the veiling glare PSF in x-ray image intensified fluoroscopy *Med. Phys.* **11** 172–9

Sempau J, Badal A and Brualla L 2011 A PENELOPE-based system for the automated Monte Carlo simulation of clinacs and voxelized geometries—application to far-from-axis fields *Med. Phys.* **38** 5887–95

Shaw R 1978 Evaluating the efficiency of imaging processes *Rep. Prog. Phys.* **41** 1103–55

Shen S, Bloomquist A K, Mawdsley G E and Yaffe M 2006 Effect of scatter and antiscatter grid on the performance of a slot-scanning digital mammography system *Med. Phys.* **33** 1108–15

Siewerdsen J H, Antonuk L E, El-Mohri Y, Yorkston J, Huang W, Boudry J M and Cunningham I A 1997 Empirical and theoretical investigation of the noise performance of indirect detection, active matrix flat-panel imagers (AMFPIs) for diagnostic radiology *Med. Phys.* **24** 71–89

Siewerdsen J H and Jaffray D A 2000 Optimization of x-ray imaging geometry (with specific application to flat-panel cone-beam computed radiography) *Med. Phys.* **27** 1903–14

Veldkamp W J H, Thijssen M A O and Kerssemeijer N 2003 The value of scatter removal by a grid in full field digital mammography *Med. Phys.* **30** 1712–8

Wagner R F, Bernes G T and Askins B S 1980 Effect of reduced scatter on radiographic information content and patient exposure: a quantitative demonstration *Med. Phys.* **7** 13–8

Yester M V, Barnes G T and King M A 1981 Experimental measurements of the scatter reduction obtained in mammography with a scanning multiple slit assembly *Med. Phys.* **8** 158–62

Young K C, Cook J J H, Oduko J M and Bosmans H 2006 Comparison of software and human observers in reading images of the CDMAM test object to assess digital mammography systems *Proc. SPIE* **6142** 614206

Zhao W and Rowlands J A 1997 Digital radiology using active matrix readout of amorphous selenium: theoretical analysis of detective quantum efficiency *Med. Phys.* **24** 1819–33